Rhythm-Based Power Allocation Strategy of Bionic Tail-Flapping for Propulsion Enhancement

Biao Wu, *Student Member, IEEE*, Chaoyi Huang, *Student Member, IEEE*, Xiangru Li, *Student Member, IEEE*, Jiahao Xu, *Student Member, IEEE*, Sicong Liu, *Member, IEEE*, James Lam, *Fellow, IEEE*, Zheng Wang, *Senior Member, IEEE*, and Jiansheng Dai, *Fellow, IEEE*

***Abstract*—With the vast demand in marine development, robotic fish show promising potential in underwater exploration for their high-performance propulsion ability. However, fish-inspired robots are yet to utilize the structural flexibility of rhythmic actuation such as bony fish (Osteichthyes). The Body and Caudal Fin (BCF) locomotion in fish optimizes the use of muscle power and body flexibility by synchronizing muscle activation with the undulating-oscillatory tail-flapping, such as Thunniform, while robotic fish are primarily designed as motion trackers rather than as efficient swimmers. In this article, we propose a power allocation strategy (PAS) that imitates muscle rhythmic actuation, which increases the flapping amplitude by the coupling of the peduncle motion and the tail deformation. Inspired by this peduncle-tail mechanism, we developed a direct-drive fish robot (DDRFishBot). The DDRFishBot is enhanced by our developed PAS in tail-elastic potential energy release by 228%, in propulsion by 45.6%, and in efficiency coefficient by 16.3%. This study establishes the performance enhancement principle of exploiting tail flexibility through a simple scotch yoke mechanism, expanding the performance space of fish-inspired tail-flapping swimming robot.**

Received 12 March 2025; accepted 24 May 2025. Date of publication 9 June 2025; date of current version 30 June 2025. This work was supported in part by the National Key R&D Program of China under Grant 2022YFB4701200, National Natural Science Foundation of China under Grant 52475302, in part by the Shenzhen Science and Technology Program under Grant JCYJ20220530114615034, Grant JCYJ20220818100417038, and Grant ZDSYS20220527171403009, in part by the University high level of special funds under Grant G03034K003 of Southern University of Science and Technology, Guangdong Provincial Key Laboratory of Intelligent Morphing Mechanisms and Adaptive Robotics under Grant 2023B1212010005, in part by the Strategic Topics Grant of Research Grants Council under Grant STG1/E-401/23-N, and in part by the CRCG under Grant 2302101740. This article was recommended for publication by Associate Editor L. Wen and Editor A. Menciassi upon evaluation of the reviewers' comments. *(Biao Wu and Chaoyi Huang contributed equally to this work.) (Corresponding authors: Sicong Liu; Jiansheng Dai.)*

Biao Wu, Jiahao Xu, and Jiansheng Dai are with the Department of Mechanical and Energy Engineering, Shenzhen Key Laboratory of Intelligent Robotics and Flexible Manufacturing Systems, Southern University of Science and Technology, Shenzhen 518055, China (e-mail: 12132303@mail.sustech.edu.cn; 12132312@mail.sustech.edu.cn; daijs@sustech.edu.cn).

Chaoyi Huang and James Lam are with the Department of Mechanical Engineering, The University of Hong Kong, Pokfulam, Hong Kong SAR (e-mail: u3562918@hku.hk; james.lam@hku.hk).

Xiangru Li is with the Department of Mechanical and Aerospace Engineering, The Hong Kong University of Science and Technology, Kowloon, Hong Kong SAR (e-mail: xlihh@connect.ust.hk).

Sicong Liu is with the Sino-German College of Intelligent Manufacturing, Shenzhen Technology University, Pingshan 518118, China (e-mail: liusicong@sztu.edu.cn).

Zheng Wang is with the Wisson Robotics, Shenzhen 518001, China (e-mail: zheng.wang@ieee.org).

This article has supplementary downloadable material available at https://doi.org/10.1109/TRO.2025.3577985, provided by the authors.

Digital Object Identifier 10.1109/TRO.2025.3577985

***Index Terms*—Bionic robot, fish swimming, robot actuation, tail flapping.**

I. Introduction

With the surge in ocean exploration, the expanse and resistance of the aquatic environments pose significant challenges for underwater equipment in long-distance cruising, hovering for observation, and high payload capability [1], [2], [3], [4], [5]. Researchers take inspiration of marine animals to design bionic robots, aiming for extensive spatial locomotion and effective power transformation. Compared to the conventional propeller, marine animals, particularly fish, have evolved exceptional swimming abilities in aquatic environments over millions of years, exhibiting remarkable efficiency, speed, and maneuverability [6], [7], [8], [9]. Besides, bionic propulsion has great adaptability in complicated and unstructured areas, which makes fish an outstanding model for developing high-performance swimming robots by exploiting their intrinsic mechanisms.

In decades, researchers embarked on a thorough study of fish, especially body-caudal fin (BCF) swimmers, focusing on the tail-flapping mechanism, for a deeper understanding of the biomechanical principles in underwater propulsion [10], [11], [12], [13]. Lighthill proposed the elongated body theory (EBT), indicating the relationship between linear velocity of the tail tip and propulsion [14]. The robotic experiments and fluid dynamics analysis simplify the caudal fin motion to a flexible beam model, aiming to elucidate the impact of actuation pattern, tail structure, and surrounding vortex on propulsion force and efficiency [15], [16], [17], [18], [19], [20], [21], [22], [23], [24]. Based on the quantitative analysis, it has been found that the mechanical resonance of the flexible tail can maximize the tail-flapping amplitude and reduce the mechanical cost of the actuation [25], [26], [27].

However, there is still a gap between the propulsion capability of robots and fish. The robot has not fully replicated the capability of fish in biomechanical coordination, while the basic propulsive components, muscle (motor), myotome (transmission), and tail (propeller) of fish are instinctively coordinated [28], [29], [30]. But the current acknowledgment of mechanical resonance is yet sufficient to explain the comprehensive biomechanical behaviors of how the body flaps the tail through coordinating rhythmic drive and structural flexibility [31], [32]. While the energy required for swimming in fish is temporarily stored in the

body as elastic energy and transformed to propulsion through the tail, robotic fish primarily focus on mimicking the body shape through mechanical deformation with rarely investigation about the energy transformation mechanism [7], [8], [33], [34], [35], [36], [37], [38]. Biological studies point out that the activation pattern of fish muscle is tailored to specific swimming mode to ensure the power transformation from muscle contraction to tail-flapping, showing a potential and uninvestigated enhancement mechanism by combining rhythmic actuation and structure flexibility [36], [39], [40].

To explore this problem, researchers are trying to synergize the rhythmic actuation and tail flexibility on the bionic robot to exploit uncovered performance potential. Unlike rigid robots are restricted by prescribed input, bionic robots with compliant components naturally produce organism-like responses through environmental interaction, which allows researchers to validate the biological hypothesis through engineering methods [34], [41], [42], [43]. Combining structural modeling and multimodal data acquisition, the effects of locomotor configurations on performance can be quantitatively compared. Based on that, this yielded numerous achievements, promoting the development of underwater bionic robots and the understanding of the intrinsic mechanism in underwater propulsion [15], [44], [45], [46], [47], [48], [49], [50], [51], [52], [53], [54], [55], [56]. Zhong et al. [57] reported that the muscle tension of the tuna-like robot should scale with the square of swimming speed to maximize efficiency. Zhu et al. developed a high-frequency robotic platform, Tunabot, based on yellowfin tuna and Atlantic mackerel to explore the performance space of high-frequency fish swimming [58]. Thandiackal et al. [59] demonstrated that a robot mimicking the neuromechanical system of undulatory swimmers can achieve self-organized swimming through local hydrodynamic force sensing. These novel mechanical designs and control strategies make the bionic robot recreate and utilize the intrinsic swimming mechanism involving body-structural elastic vibration to enhance propulsion. Previously, our group developed a series of underwater soft robots based on the simple yet effective bioinspired principles [60], [61], [62], [63]. Among them, the Big Bay Fish [64] broke the Guinness World Record for the fastest swimming robotic fish in a 50 m pool with a time of 22.16 s, by utilizing a synergy method between peduncle motion and tail-flapping for the first time, which is considered as a key factor for self-exploited performance enhancement. Considering the promising potential, here we uncover the coupling between rhythmic actuation and tail flexibility to establish a bioinspired control strategy that imitates intrinsic biomechanical coordination for propulsion enhancement of fish-inspired tail-flapping swimming robot.

This article focuses on the coupling effect between the peduncle motion and tail vibration, where the passive rebound behavior of the tail brings benefits for the robotic fish propulsion. By controlling the power allocation of driving motor, the rebound of the flexible tail can be regulated to improve the tail-flapping amplitude and hence the propulsion performance. A deformation model is derived to describe the tail-flapping and tail-elastic potential energy (T-EPE) under rhythmic actuation. A bioinspired prototype is developed with a peduncle-tail direct-drive mechanism, achieving superior performance compared to state-of-the-art works, described by the nominal thrust to input ratio (NTIR), without adding extra controllable hardware. The main contributions are as follows.

1) We proposed a power allocation strategy (PAS) based on rhythm actuation for bionic fish that can regulate the coupling effect between the peduncle motion and the tail vibration to enhance propulsion.
2) A deformation model describing the tail-flapping pattern under rhythmic peduncle actuation is derived based on the pseudorigid-body model (PRBM), through which the relationship between the tail elastic vibration and propulsion enhancement is obtained.
3) Drawing inspiration from the peduncle-tail mechanism, a direct-drive fish robot (DDRFishBot) is developed for experimental validation. By utilizing the inherent structural flexibility of the tail, the DDRFishBot can enhance and expand the controllable space of propulsion performance, without the need for additional drive mechanisms for body deformation or stiffness adjustment.

The rest of this article is organized as follows. Section II presents the bioinspiration and modeling of rhythm actuation. Section III includes the design and fabrication of the DDRFishBot, along with experimental setup and data processing procedure. Section IV validates the impact of rhythmic characteristics on the bionic propulsion mechanism. Finally, Section V concludes this article.

II. Modeling of Tail-Flapping Strategy

A. Muscle Activation Pattern of Fish Swimming

BCF swimmers undulate the body to push the water by the coordination of power generation and transmission through muscle contraction [10]. As shown in Fig. 1(a), previous studies have pointed out that muscles in various parts of the fish would actuate rhythmically in sequence [65]. Down the length of fish, the posterior muscle and the caudal peduncle mainly perform stiffness regulation to transmit the mechanical power from the anterior muscle to drive the tail. Inspired by this, a bionic peduncle-tail mechanism is adopted to imitate the rhythmic actuation characteristics of fish swimming, as shown in Fig. 1(b). We set a novel rhythm controller to regulate the power output of a dc motor with respect to the flapping angle of peduncle actuation. The anterior torque is transmitted through a scotch yoke mechanism and a rigid peduncle to deform a flexible tail under hydrodynamic force.

As shown in Fig. 1(c), the muscle activation is related to the muscle strain patterns underlying the bending of the fish body. The strategies to perform tail-flapping through muscles vary among fish species [36]. Functional differences in muscular motion occur in the longitudinal direction. The duration of muscle activation decreases towards the tail while electromyography onset occurs earlier in more posterior area. The phase between the strain and activation cycle determines the power generated by the muscle. For species that generate propulsion at the tail, the muscle power must be transferred to the tail for propulsion generation, so that the posterior muscle may stiffen to aid power transmission. During this process, it has been proven that the stiffening of muscle can produce the maximal power output for

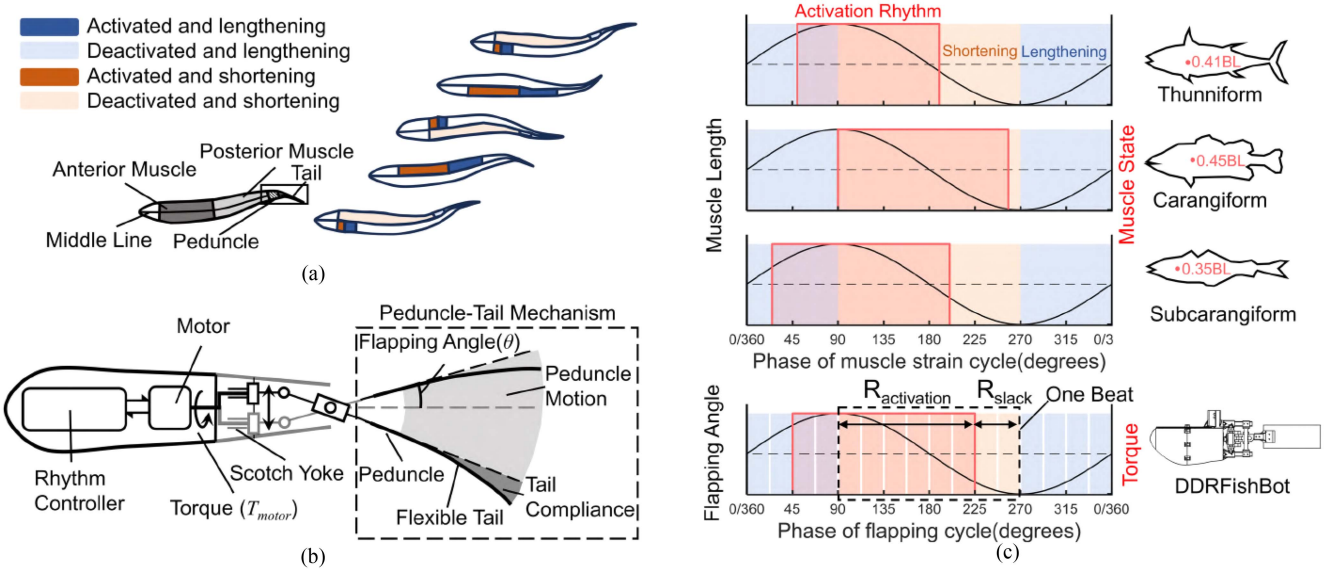

Fig. 1. Fish activate muscles in sequence to generate propulsion. (a) Anterior muscles contract for power generation while the posterior muscle and caudal peduncle primarily regulate stiffness to transfer the mechanical power to the tail. (b) Scheme of the bionic fish with peduncle-tail mechanism, with a rhythmic actuation of dc motor and scotch yoke transmission. (c) Activation rhythm of the anterior muscle is restricted to specific fish species, while the DDRFishBot can switch the drive pattern in a wider range. The position of fish anterior muscle is expressed as a proportion of the body length (BL).

propulsion generation. However, the relationship between the anterior muscle activation and swimming pattern is not entirely clear due to the limitations of biological in vivo experiments.

Benefiting from the engineering approach, the robotic propeller can easily adjust the actuation pattern of the tail-flapping in a wide range. Based on the discretized allocation of modulated motor actuation, the rhythmic variation for imitating desired muscle activation patterns is given by

$$R_{\text{power}} = R_{\text{activation}} - R_{\text{slack}}$$
$$= S_a - S_s[u(\text{sign}(\dot{\theta})\theta - \theta_s) - u(\text{sign}(\dot{\theta})\theta - \theta_s - \theta_d)] \quad (1)$$

where $R_{\text{activation}}$ and R_{slack} represent the activation, and slack components of the muscle activation patterns, respectively, S_a is the activation level, S_s is the slackness level, θ is the flapping angle, $\dot{\theta}$ is the derivative of θ, θ_s, and θ_d are the start timing and the duration of the slack within a cycle, respectively, u denotes the step function. Therefore, the rhythm controller of DDRFishBot can be switched to regulate the actuation of the proposed peduncle-tail mechanism to explore how the anterior power can be effectively converted into propulsion through flapping the flexible tail.

B. Modeling of Peduncle-Tail Mechanism

In this section, the peduncle-tail mechanism and the rhythmic characteristics of the peduncle actuation are modeled for propulsion estimation. First, the deformation of the flexible tail under the hydrodynamic force can be treated as a forced beam deflection problem. However, the nonlinearity of a large deformation beam makes it difficult to solve. Therefore, the PRBM method was adopted to calculate the deformation of the caudal fin under a given peduncle actuation. Fig. 2(a) illustrates the peduncle-tail mechanism with a coordinate system XOY set at the center of tail-flapping motion. A model based on 3R PRBM is developed,

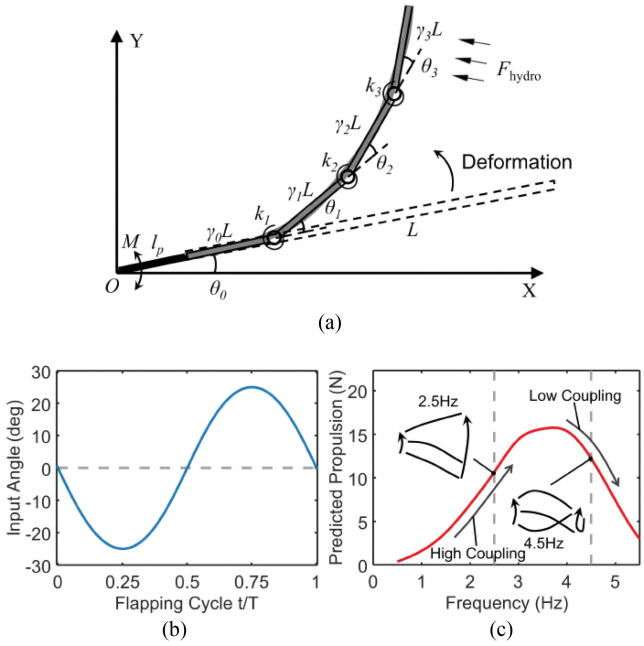

Fig. 2. (a) Four-link PRBM of the peduncle-tail mechanism. (b) Conventional peduncle actuation with sinusoidal pattern. (c) The simulation result present two types of coupling effect in propulsion generation.

where the bolded link represents the mechanical motion of the rigid peduncle while the rest four links are used to fit the deformation of the flexible tail for the overall bending curve. The links satisfy the length ratio $\gamma_0 = \gamma_1 = \gamma_2 = \gamma_3 = 0.25$ and are jointed by pin joints and torsional springs with torsional spring constant $k_1 = k_2 = k_3 = K_\theta$ [66], [67]. The flexible tail is connected to the body by the rigid peduncle and bends into a C or S-shaped under the driving moment M and hydrodynamic force F_{hydro}. As shown in Fig. 2(b), the peduncle oscillates back

and forth around point O, and its rhythmic pattern is first assumed to be sinusoid as

$$\theta_0(t) = B\sin(2\pi ft + \delta) \tag{2}$$

where B is the amplitude, f is the frequency, δ is the phase lag, which represents the initiative position of the peduncle.

As the first pseudolink can be approximated as pivoting at point O, the velocity perpendicular to the first pseudolink at an arbitrary position is obtained by

$$v_{y0} = \dot{\theta_0}(t)(l_p + x), x \in [0, \gamma_0 L] \tag{3}$$

where $\dot{\theta_0}$ is the angle velocity of the peduncle, l_p is the length of the peduncle, L is the total length of the flexible tail, x represents the position along the length of one pseudolink. The velocity perpendicular to the subsequent pseudolink at an arbitrary position on it can be approximately derived as follows:

$$v_{yi} = v_{yJi-1}\cos\theta_i - x\dot{\theta}_i, x \in [0, \gamma_i L], i = 1, 2, 3 \tag{4}$$

where v_{yJi-1} is the joint velocity, which is obtained by setting $x = \gamma_{i-1}L$ in v_{yi-1}, θ_i is the deflection angle of the pseudolink, $\dot{\theta}_i$ is the deflection angle speed. The hydrodynamic force perpendicular to the tail due to the encompassing fluid is given by

$$F_{\text{hydro}} = -\frac{1}{2}\rho_w v_y(x,t)|v_y(x,t)|hC_d \tag{5}$$

where ρ_w is the density of water, h is the width of the tail, C_d is the coefficient, which describes the water damping effect on the tail.

The underwater forced vibration of the flexible tail is then obtained by the following equation, including hydrodynamic force, internal spring force, and inertial force of each segment

$$m\ddot{y} = F_{\text{hydro}} + F_{\text{spring}} \tag{6}$$

where m is the mass of pseudolink, $\ddot{y}$ represents the vertical acceleration component of the mass center of pseudolink.

Since the links of the PRBM are connected by a torsion spring, the equivalent force is given by

$$F_{\text{spring}} = \frac{EIK_\theta\theta_i}{(\gamma_i L)^2}, i = 1, 2, 3 \tag{7}$$

where E is the Yang's modulus of the beam, I is the area moment of inertia of the beam, K_θ is the nondimensional torsional spring constant.

By substituting (5) and (7) into (6), the ordinary differential equation of a single segment is derived as

$$f(\theta, v_y, \gamma) = \left(-\frac{EIK_\theta\theta_i}{\gamma_i L^2} - \frac{1}{2}\rho v_y|v_y|hC_d\right)/m. \tag{8}$$

Combining four rigid segments into the overall equation group, we can compute the deformation of the flexible tail and external load due to the hydrodynamic force. The values of the parameters in this model are shown in Tables I and II. Specifically, C_d and K_θ are derived through a least squares fit of the model predicted tail tip displacement to experimental data of constant strategy and the other values are determined by prototype design.

TABLE I
PARAMETERS OF PRBM

Parameter	Value
Damping effect coefficient C_d	0.68
Non-dimensional torsional spring constant K_θ	0.87
Yang's modulus of the beam E	$2.3 \times 10^9 Pa$
Density of water ρ_w	$1000\,\text{kg/m}^3$
Mass of a single segment m	0.0221kg
Area moment of inertia along the length of the foil I	$2.25 \times 10^{-10}\text{m}^4$
Amplitude of the flapping angle B	49.9°

TABLE II
SPECIFICATION OF THE PLATFORM

Component	Specification
Dimensions of PC foil (mm)	245 (l) × 100 (h) × 3 (b)
Density of PC foil (kg/m^3)	1200
Dimensions of water tank (m)	1.98 (L_t) × 1.4 (W_t) × 1 (H_t)
Radius of steering wheel R (mm)	15
240Hz Camera	iPhone 13 Pro 128G
6-axis force sensor	APDW-6D-110
Power supply module	Wide-range voltage stabilizer
Battery	22.2V 850mAh LiPo battery
CAN bus	Your Cee TJA1050
DC electronic speed control	RMDS-305

Based on the Lighthill model, the mean propulsion can be given by the following equation:

$$\overline{P} = \overline{\left[m_v w\left(\frac{\partial Y}{\partial t} - \frac{1}{2}w\frac{\partial X'}{\partial a}\right)\right]_{a=0}} \tag{9}$$

where m_v is the virtual mass per unit length, w is the velocity in the direction perpendicular to the tail, Y is the displacement in the perpendicular direction, X' is the displacement in the swimming direction, and a is the distance along the tail tip from the tip. Fig. 2(c) presents the envelope of one tail-flapping and the propulsion prediction under sinusoidal peduncle actuation. The propulsion exhibits a corresponding surge with frequency increasing, peaking at 3.8 Hz and then commencing a gradual decline. Despite maintaining equivalent propulsion, the ascending phase exhibits a more direct transformation of the peduncle oscillation into a linear motion at the tail tip, in contrast to a looped tip trajectory during the descending phase. In other words, the ascending phase demonstrates a superior coupling effect between the peduncle actuation and tail deformation than the descending phase, resulting in a more effective tail-flapping pattern.The EBT proposed the conditions for elongated fish to perform high propulsive efficiency, where the oscillation amplitude should increase from the head of the fish to the maximum at the tip of the caudal fin, as shown in Fig. 3(a). Equation (9) indicates that the magnitude of the propulsion depends on the velocity of the tail tip, therefore increasing the amplitude and frequency of the tail-flapping are both crucial for propulsion generation. However, the hydrodynamic force F_{hydro} would increase to bend the tail into a larger curvature with frequency increase. As depicted in Fig. 3(c), the excessive bending would counteract the peduncle actuation, which would hinder the motion transmission

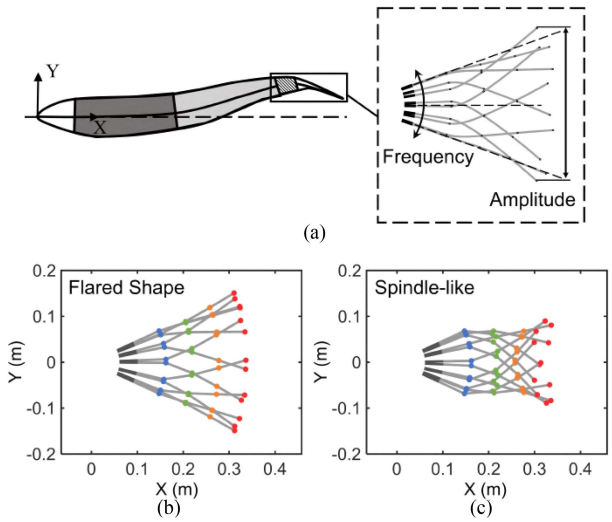

Fig. 3. (a) Propulsion is positively correlated with the linear velocity of tail tip, determined by both frequency and amplitude. The simulation result present the envelope of coupling tail-flapping, (b) flared shape and (c) spindle-like, which indicate the amplification relationship between peduncle actuation and tail tip movement.

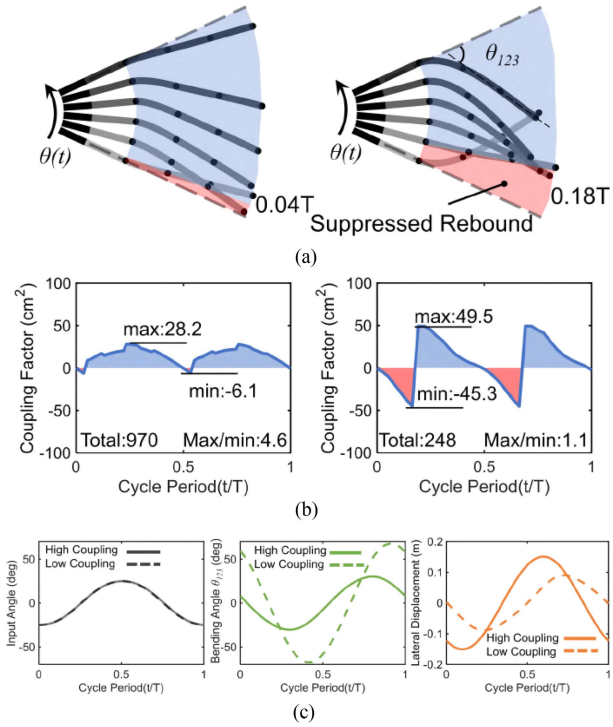

Fig. 4. (a) Tail rebound behavior. (b) Total and extremum ratio of tail-flapping coupling factor. (c) Deformation comparison under tail-flapping of flared shape and spindle-like envelope.

from the anterior motion input into the posterior movement of the tail tip, resulting in a spindle-like tail-flapping pattern with lower amplitude. In contrast, Fig. 3(b) demonstrates the tail-flapping pattern at a high coupling, exhibiting a flared shape pattern, the rebound of the tail is being utilized to flip the water, with an amplitude even wider than the input of peduncle actuation.

To quantify this performance-enhancing effect, we employed a coupling factor k_c that describes the relative motion between the peduncle and the tail. The coupling factor between tail deformation and peduncle motion is calculated as the product of three factors: the projection of the tail's bending deformation onto the extended axis of the peduncle, the flapping distance of the peduncle motion at the tail tip, and the direction of the peduncle motion as follows:

$$k_c = \dot{\theta}_0(l_p + L)\cos(\theta_{123})\text{sign}(\theta_{123})\sum_{k=1}^{3}(\gamma_k L) \tag{10}$$

where $\text{sign}(\theta_{123})$ is defined to indicate the sign of θ_{123} and $\text{sign}(0) = 1$, $\theta_{123} = \sum_{k=1}^{3}\theta_k$ is the sum of deflection angle. As shown in Fig. 4(a), the effective rebound behavior and the conflict during counter-phase motion of the peduncle and tail are shaded, respectively, in blue and red. In the tail-flapping motion, the total amount of the coupling factor k_c characterizes the strength of the coupling effect, while the extremum ratio reflects the variation within this coupling effect. As Fig. 4(b) presents, both the total amount and extremum ratio are conducive to enhancing the propulsion force generated by tail-flapping. Higher total amount indicates a more robust interaction between the peduncle and tail, thereby enhancing the interaction with the surrounding fluid. Meanwhile, higher extremum ratio is associated with pronounced variation in the coupling effect, which is conductive to the tail rebound behavior for increase in the amplitude of tail-flapping. Moreover, Fig. 4(c) demonstrates that the delayed rebound timing and larger maximal angle suppress the transformation to lateral displacement. Overall, the PRBM model reveals a coupling effect between the rhythmic actuation of the peduncle and the flexible vibration of the tail, which can be synergistic to enhance the tail tip velocity.

C. Rhythmic Actuation Coordination With Tail Vibration for Propulsion Enhancement

To explore the coupling effect between peduncle actuation and tail deformation, the influence of the peduncle actuation pattern on propulsion performance is compared. To imitate the muscle activation of fish, a dc motor directly drives the rigid transmission mechanism to build a reactive robotic system [34]. According to the biological studies about fish muscle activation patterns, two types of actuation patterns are set for comparison with the sinusoidal pattern, slacken at the terminal (TS), and slacken at the middle (MS), which are fitted by the Fourier series to avoid the possible singularity, as shown in Fig. 5(a) and (b) [68], [69], [70].

In this study, the torque and elastic energy associated with tail-flapping under conditions of high-coupling and low-coupling are examined. Specifically, the variations in T-EPE and the hydrodynamic torque exerted on the tail are analyzed as a function of the tail-flapping cycle. The magnitude of the change in T-EPE from its maximum value to the end of the cycle serves as an indicator of the tail rebound effect. Notably, the TS strategy exhibits the most significant rebound effect during both tail-flapping phases, which are demarcated by the neutral position of the peduncle motion.

The propulsion prediction under modulated patterns is shown in Fig. 5(c) and exhibits a corresponding modulation on the propulsion generation. Compared to the conventional sinusoid

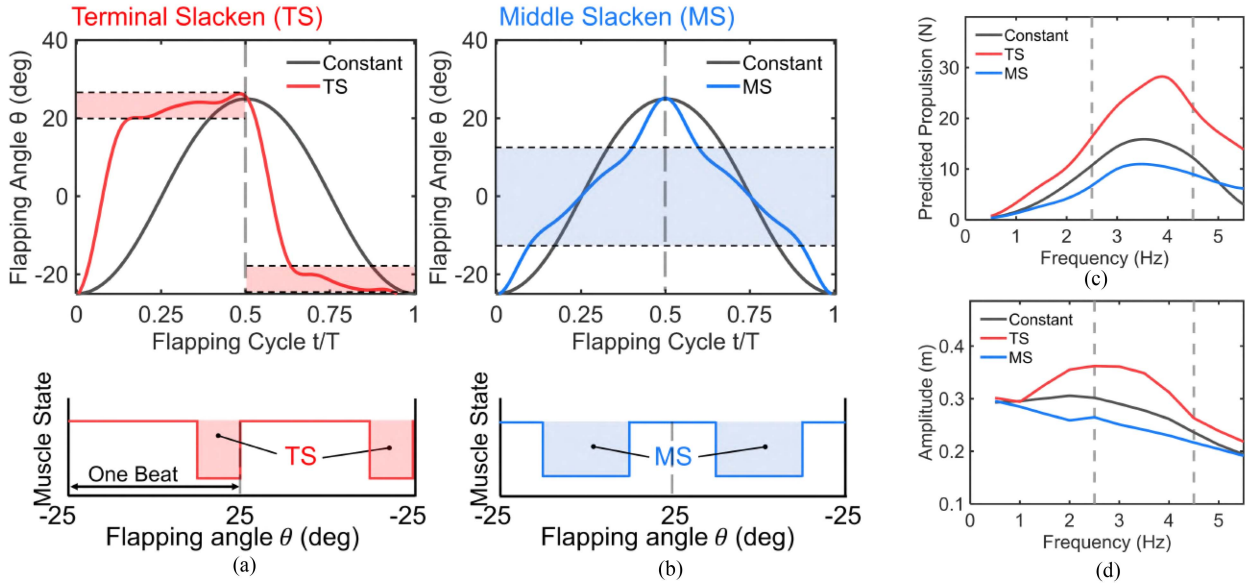

Fig. 5. Utilizing the modified rhythmic actuation patterns of (a) Terminal Slacken and (b) Middle Slacken, the simulations demonstrate a corresponding regulation effect in the (c) predicted propulsion and (c) amplitude.

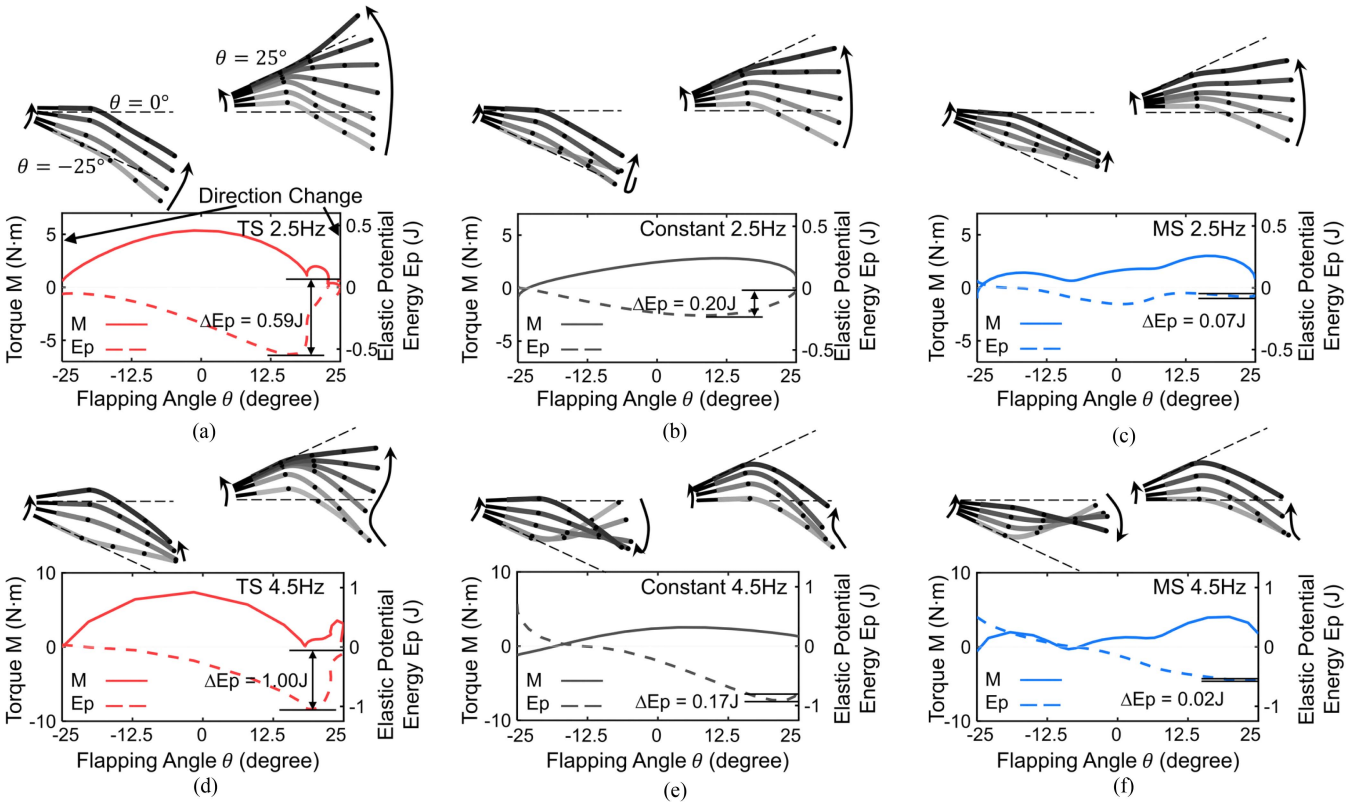

Fig. 6. Tail, actuated by the peduncle, accumulates T-EPE in its anterior segment and subsequently releases it in the posterior period into tail tip movement. The simulation demonstrates the variations in T-EPE and hydrodynamic torque under the frequency (a)–(c) 2.5 Hz and (d)–(f) 4.5 Hz with TS, constant, and MS strategy.

rhythm, the modulated actuation pattern expands the performance space of the peduncle-tail mechanism. In Fig. 5(d), the observed difference in amplitude is consistent with the increase in the lateral motion of Y at frequency f, corresponding to (9). This concordance verifies that the enhancement and reduction of propulsive force are indeed attributed to variations in amplitude. As depicted in Fig. 6, the deformation of tail-flapping is bifurcated into two half-cycles centered on the midline. Based on the modulation of the propulsive gait, the propulsion generated by tail-flapping can be modulated by the rhythmic pattern of the

peduncle actuation. Theoretically, without a complex mechanical structure, a simple scotch yoke mechanism can perform similar propulsion modulation ability to multijoint or stiffness-tuning mechanism.

Furthermore, to investigate the effects of high and low-coupling conditions on the propulsive force, we selected the tail-flapping at 2.5 Hz and 4.5 Hz as representations for analysis. Fig. 6 presents the variations in T-EPE and hydrodynamic torque acting on the tail during the tail-flapping cycle. Furthermore, the process of tail-flapping was visualized, with the neutral plane as the demarcation point. Notably, the TS strategy facilitated a more comprehensive release of T-EPE in the latter half of the tail-flapping before the direction change, enabling a more pronounced rebound effect and amplitude increase. As depicted in Fig. 6(a) and (d), the amount of T-EPE released between the peak and direction change was 0.58 J at 2.5 Hz and 1.2 J at 4.5 Hz, respectively. It was 290% and 706% higher than that observed in the constant strategy. As for MS strategy, the difference was enlarged further to 1160% and 3000%.

The tail-flapping pattern is a combination of the peduncle actuation and tail deformation. The bending curve is determined by the force balance between the peduncle, tail, and water, where the transition of elastic potential energy serves to store and re-release the mechanical power. As shown in Fig. 6(a), during the flapping cycle, the T-EPE is transitioned with respect to the relative motion between the tail and the water. It first bends and stores T-EPE in response to peduncle actuation and hydrodynamic force during acceleration. Then, it decelerates and tends to return to the neutral state at the end of one beat, converting the T-EPE into a force onto the water. The TS mode has the maximum release of elastic potential energy at the limiting positions on both sides and the rebounding of the tail can additionally beat the water. For the MS and sinusoidal modes, the tail fails to complete the rebounding, whose local deformation is opposite to the direction of the peduncle actuation after the reversal of direction, further weakening the relative motion with the water. The utilization of the inherent flexibility through rhythmic actuation can help the power transmission from the anterior motor to the posterior tail, increasing the velocity of the tail tip with respect to the peduncle actuation input.

Moreover, the comparison of coupling effect between these three typical strategies (TS, constant, and MS) at high coupling (2.5 Hz) and low coupling (4.5 Hz) states is shown in Fig. 7. Compared with Fig. 4, TS strategy shows the leading coupling effect in total amount, extremum ratios, and corresponding propulsion performance enhancement in both states. Overall, our model introduces the rhythmic variation of the peduncle actuation into the propulsion model, which can be used to enhance the propulsion performance. The rhythmic pattern can modulate the tail vibration to synergize with the peduncle actuation for the utilization of inherent flexibility.

III. Design and Experiment of Rhythm-Based Actuation

To verify the model prediction, the DDRFishBot is designed for experimental validation. Then, a rhythm-based actuation method and motion transmission mechanism based on scotch yoke are developed. Finally, a multimodal sensing framework and experimental platform are set up to collect the internal states of motor and external locomotor gaits.

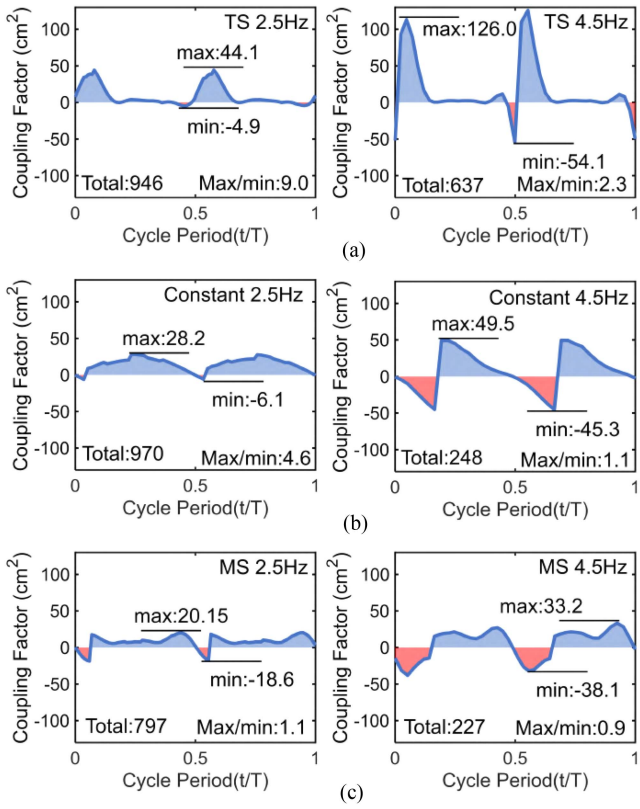

Fig. 7. Total and extremum ratio of coupling factors for TS, constant, and MS strategies (a)–(c) at 2.5 Hz and 4.5 Hz.

A. Design of the DDRFishBot

As shown in Fig. 8(a), a dc motor (MAXON RE40) was employed at the anterior body. The lateral reciprocating mechanism rotates around the fixed lever axis forming a lever to amplify the tail movement. The middle end of the actuator rod is slotted so that it is movable during the flapping to avoid self-locking. The rotation was converted into lateral reciprocating motion by the scotch yoke mechanism. Then, it drove both the rigid linkage and the attached flexible caudal fin to swing in the water through the lever structure. The schematic illustration is shown in Fig. 8(b). The appearance of the DDRFishBot is presented in Fig. 8(c), wherein the electrical supply and control mechanisms are achieved via a tether, enabling unhindered connectivity. Notably, a rigid frame is incorporated to ensure sufficient payload capacity, facilitating the attachment of the DDRFishBot to a stationary platform. This allows for the effective transmission of propulsion to force sensors, thereby enabling convenient observation of tail deformation and propulsion generation. Besides, a rectangular flexible foil is adopted to simplify the complex three-dimensional geometry of the fish, focusing on the effects of different rhythmic actuation patterns on the tail-flapping pattern and propulsion generation [71].

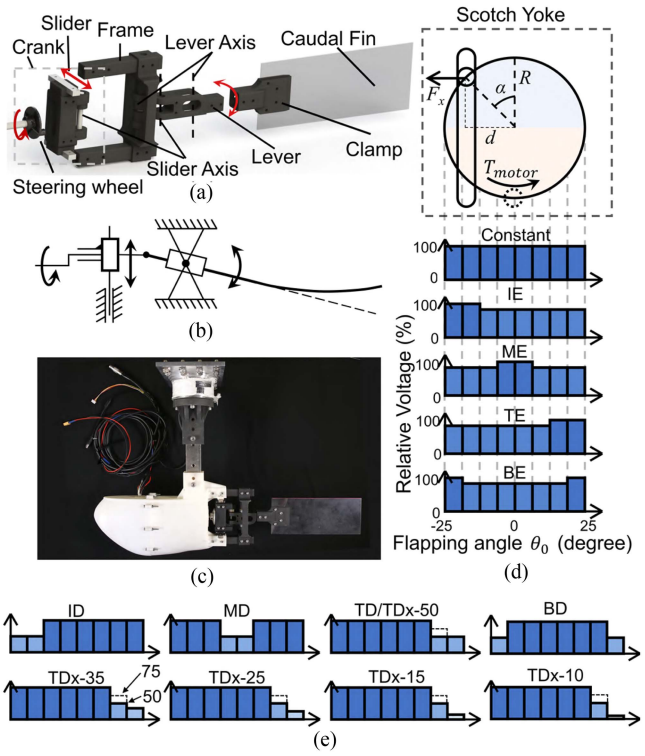

Fig. 8. (a) Motor rotation is converted into lateral oscillation and amplified by the lever between the slider and fixed axis. (b) Schematic illustration of the motion transmission mechanism. (c) Prototype of DDRFishBot. (d) Implementation of the power output between the voltage input and the rotation angle of the scotch yoke mechanism. (e) Voltage pattern of decline strategy and TD strategy.

B. Rhythm-Based Voltage Regulation for PAS

To perform the modified rhythmic actuation, a PAS was conducted to map the power regulation of the motor to the tail-flapping, as shown in Fig. 8(d). Given that the motion transformation of the scotch yoke mechanism is inherently reliant on the rotation angle, a positional mapping is derived between the electric motor and the peduncle motion.

The relationship of kinematic and dynamics between the rotation and the horizontal projection of the steering wheel are shown in Fig. 8(d) and follow the equation

$$d = R\sin(\alpha) \tag{11}$$

$$F_x = T_{\text{motor}}/R\cos(\alpha) \tag{12}$$

where d is the horizontal projection position of the steering wheel, F_x is the horizontal force, R is the radius of the steering wheel, T_{motor} is the torque onto the steering wheel, and α is the angle of the rotation. Then, the power projection of the motor in the horizontal direction is given by

$$P_{\text{output}}(\theta_0) = F_x\dot{d} = T_{\text{motor}}\cos^2(\alpha). \tag{13}$$

Based on that, we designed a series of strategies that can adjust the voltage input at four positions: initial, middle, terminal, and bipolar. The specific parameters for the driving strategy are shown in Table III. Here, E (Elevation) and D (Decline) represent the change in motor voltage to generate acceleration and deceleration of the scotch yoke slider, respectively. Meanwhile,

TABLE III
VOLTAGE PATTERN OF PAS

Description	Abbreviation	PAS
Constant	Constant	100,100,100,100,100,100,100,100
Initial decline	ID	50,50,100,100,100,100,100,100
Initial elevation	IE	100,100,83,83,83,83,83,83
Terminal decline	TD	100,100,100,100,100,100,50,50
Terminal elevation	TE	83,83,83,83,83,83,100,100
Mid decline	MD	100,100,100,50,50,100,100,100
Mid elevation	ME	83,83,83,100,100,83,83,83
Bipolar decline	BD	50,100,100,100,100,100,100,50
Bipolar elevation	BE	100,83,83,83,83,83,83,100

TABLE IV
VOLTAGE PATTERN OF TD STRATEGY

Abbreviation($x = 75, 50$)	PAS
TDx-50	100,100,100,100,100,100,x,50
TDx-35	100,100,100,100,100,100,x,35
TDx-25	100,100,100,100,100,100,x,25
TDx-15	100,100,100,100,100,100,x,15
TDx-10	100,100,100,100,100,100,x,10

I (Initial), M (Middle), T (Terminal), and B (Bipolar) represent the position of PAS. The tail-flapping undergoes eight intervals between two limit points. Each force interval is assigned a numerical value to control the motor voltage as a proportion of the peak voltage, generating various PAS. Furthermore, given the superior performance enhancement exhibited by the model predictions in reducing terminal velocity, an additional control group is introduced for the TD strategy, focusing on the motor voltage pattern. The details of this control group are presented in Table IV and illustrated in Fig. 8(e).

C. Multimodal Data Acquisition

As shown in Fig. 9, a multimodal data acquisition framework was designed to evaluate the performance of the DDRFishBot. Internal state, along with external locomotor behavior, is collected and analyzed through the host computer. The microcontrol unit (STM32f103C8T6) connects the host computer and the underlying driver. It receives the voltage pattern from the host computer, executes the PAS in real time, and the encoder (OID-C3815S24S) returns the current and encoder signals. Besides, since the qualitative relationship of the tail-flapping parameters given in (9), the propulsion is affected by both lateral deformation and tail beat frequency.

D. Visual Processing

Video processing was applied to capture the trajectory of the tail-flapping for gait analysis. As shown in Fig. 10, the video was then intercepted with 10 images at the beginning of the experiment for feature capture. The flexible tail was first manually labeled for training a decision tree model that was adopted to avoid environmental interference. With the RGBHSV data of the corresponding points, the trained decision tree can distinguish the pixel points of the flexible tail during the rapid flapping motion. Finally, the recognized pixel points are fitted through

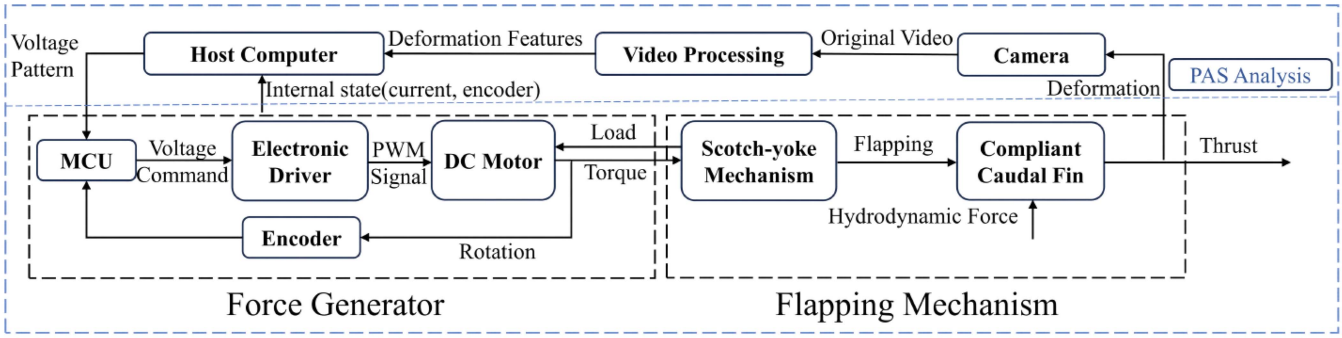

Fig. 9. Schematic diagram of the experimental validation on DDRFishBot. The host computer sends the voltage pattern to the microcontroller. The internal state of dc motor and deformation of tail-flapping is recorded by the upper level computer.

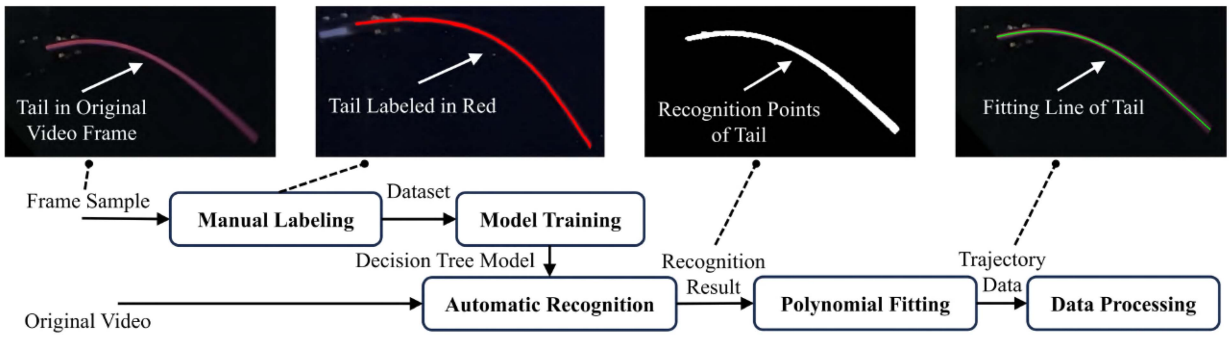

Fig. 10. Trajectory recognition of the tail-flapping pattern with fluorescent staining.

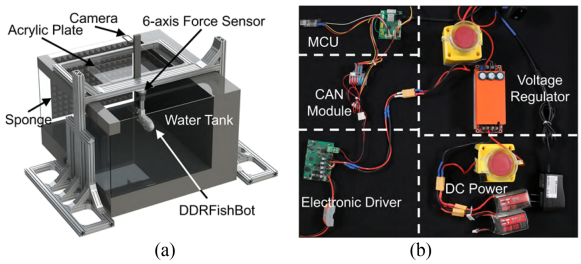

Fig. 11. Prototype was set in hydrostatic start-up conditions with multimodal information collection. (a) Water tank equipped with sound-absorbing cotton, 6-axis force sensor and a camera module fixed at the top. (b) Prototype is controlled by a tethered power supply system and host computer. The regulator amplifies and stabilizes the output of two LiPo battery at 46.4 V to prevent the voltage reduction as the battery charge drops.

quadratic polynomial fitting for further quantitative analysis of the tail-flapping pattern.

E. Experimental Platform

To investigate the effects of PAS, we have developed an experimental platform and mounted the DDRFishBot onto it for the purpose of evaluating its propulsion performance. The DDRFishBot was connected to a 6-axis force sensor (APDW-6D-110, Aanhui Epic Electronic Technology Company, Ltd.) by a steel rod to be fixed on a stand and submerged in a tank of water with dimensions listed in Table II, with sound-deadening cotton around the tank to counteract waves, as shown in Fig. 11(a). The force sensor was sampled at 500 Hz frequency and measured forces were converted to the static propulsion of the robotic fish.

Based on that, the static propulsion of the flexible tail can be used to estimate the swimming speed, by setting the static propulsion $\overline{P}$ is roughly equal to drag force F_D [6], [72]. The speed can be expressed as

$$V = \sqrt{\frac{2\overline{P}}{\rho_w S C_D}} \tag{14}$$

where V is the forward speed, S is the wetted surface area of the foil, and C_D is the drag coefficient. Given the estimated speed and propulsion, the output power P_{out} of the flexible tail can be expressed as

$$P_{\text{out}} = \overline{P}V = \sqrt{\frac{2\overline{P}^3}{\rho_w S C_D}}. \tag{15}$$

For the same tail, the values of S and C_D remain constant. By setting the S and C_D as 1, an efficiency coefficient for the qualitative assessment is expressed as

$$\eta = \frac{\sqrt{\overline{P}^3}}{\overline{U}\overline{I_c}} \tag{16}$$

where U is the voltage and I_c is the current of motor. A higher value of η indicates greater efficiency in transferring energy from electrical input to propulsion output.

Besides, a high-speed camera was mounted at the top of the shelf, and videos were captured at 240 Hz through a transparent

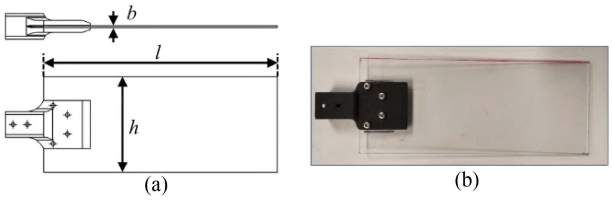

Fig. 12. (a) Diagram. (b) Prototype of the PC foil.

acrylic panel used to suppress the water splashes. The top of the flexible caudal fin was stained with fluorescent paint and lighted using a UV lamp, with a black cloth to mask external light for clear identification. As shown in Fig. 9, the DDRFishBot is powered and controlled by an external electronic system. Fig. 11(b) presents electrical system including safety switches, voltage regulator module, LiPo battery, CAN bus, and dc, whose detailed information is listed in Table II. The flexible tail adopted in this article is composed of a rigid 3D-printed nylon clamp and a PC foil, as shown in Fig. 12(a) and (b).

IV. Analysis of Power Allocated Tail-Flapping

A. Validation of Rhythm-Based Actuation Method

In the experiments of this article, the voltage input is settled at 5.8 to 46.4 V with a 5.8 V interval, to test the propulsion performance of the DDRFishBot. First, the conventional constant voltage control is used as the comparison group, labeled by the grey shade. Fig. 13(a) presents the propulsion characteristics that increase with frequency, enter a plateau at 2 Hz, and then resume the growth trend at 5 Hz. These characteristics can be divided into three stages.

During stage I, the propulsion grows linearly with the frequency, with an efficiency peak at 2 Hz as shown in Fig. 13(b). In stage II, the propulsion growth is influenced by the rapid decrease in amplitude, as shown in Fig. 13(c). When the decline in magnitude levels off, the propulsion generation enters stage III and the effect of changes in tip displacement on the linear velocity of the tail tip is reduced when the effect of frequency dominates in the propulsion generation.

As depicted in Fig. 13(d)–(f), the implementation of rhythmic actuation significantly broadens the performance envelope attainable by the flexible tail. In alignment with the model predictions, the TD strategy exhibits the most significant and optimal effect among these approaches. The PAS regulated the characteristics of the propulsion generation by modifying the tail-flapping amplitude. Further examination of TD strategy is presented in Fig. 13(g)–(i), obtaining an optimal propulsion enhancement with Δ Amplitude = 30.0 mm and ΔEfficiency Coefficient= 1.26. Although the voltage regulation of PAS causes a frequency reduction, the DDRFishBot still achieves maximum propulsion enhancement of 45.6% from the peak of the constant strategy, as shown in Fig. 13(g). Although the reduction in total power lowered the frequency, the 14.2% amplitude increment compensated for the reduction in frequency as shown in Fig. 13(i). The tail-flapping deformation illustrated in Fig. 14, along with the simulation of the tail tip trajectory, demonstrates the regulation effect of the PAS on tail-flapping. Specifically, the lateral movement of the tail gradually increases from the peduncle to the tip, aligning with the ideal tail-flapping conditions based on the EBT.

To quantify the performance enhancement on DDRFishBot, the proposed PAS is compared with state-of-the-art propulsion methods, such as stiffness adjustment, hydraulic stiffness sequencing, and shape-morphing deformation control, in terms of both the NTIR and number of controllable hardware [26], [72], [73], [74]. As shown in Table V, the DDRFishBot with direct-drive mechanism and PAS achieves an NTIR of 60.89 (N/Hz/kw). This indicates a 91.9% enhancement over the closest comparison, while simultaneously maintaining the least number of controllable components.

B. Analysis of Tail-Flapping Kinematics

To further explore the effect of the PAS configuration on propulsion performance, a kinematics analysis was conducted on the tail-flapping pattern. Fig. 15(a)–(c) demonstrates the hydrodynamic torque, T-EPE, and deformation pattern of tail-flapping under three strategies. As the frequency increases, the tail vibration shifts from the first-order to the second-order mode, accompanied by a decrease in the tail-tip amplitude, resulting in a narrowing envelope. The deformation of the flexible tail is influenced by the driving moment and hydrodynamic force.

The relative movement of the peduncle to the tail is the key to uncovering the rhythm coupling effect. The peduncle motion first precedes the tail motion, which causes the tail to bend and accumulate T-EPE. This process continues until the bending of the tail reverses over the peduncle and transfers energy to the environment. Eventually, the accumulation and release of T-EPE will begin again during the next tail-flapping cycle. The adequacy of the time window is crucial for the tail to rebound. Specifically, it is directly correlated with the increment of amplitude at the end of the tail-flapping. Therefore, the TD75-15 strategy obtains the best improvement among our previously tested group. The TD75-15 strategy attains a maximum $\triangle$ Ep of 0.394J within one tail-lapping, which exceeds 200% in comparison with the constant and MD strategies. A slowed downward trend of the torque also presents an increase in water interaction by the T-EPE release. It also reaches the middle of the flapping angle at an earlier time, 0.159 T, resulting in a 14.8% lateral displacement improvement, as shown in Fig. 15(d)–(f). Differential driving velocities at the peduncle optimize the storing and releasing of T-EPE. The reduction at the terminal of each beat can slow down the peduncle motion, enhancing the transformation from the T-EPE into hydrodynamic forces. However, an inappropriate actuation pattern weaken the utilization of tail compliance, with a lower storage level and an insufficient release window, such as TD75-15 and MD strategy.

C. Statistical Evaluation of Rhythm Coupling

To identify the parameters affecting propulsion generation, a statistical evaluation was performed to quantify the tail-flapping motion under environmental interaction. Fig. 16 shows the flapping speed of the tail under TD75-15, constant, and MD

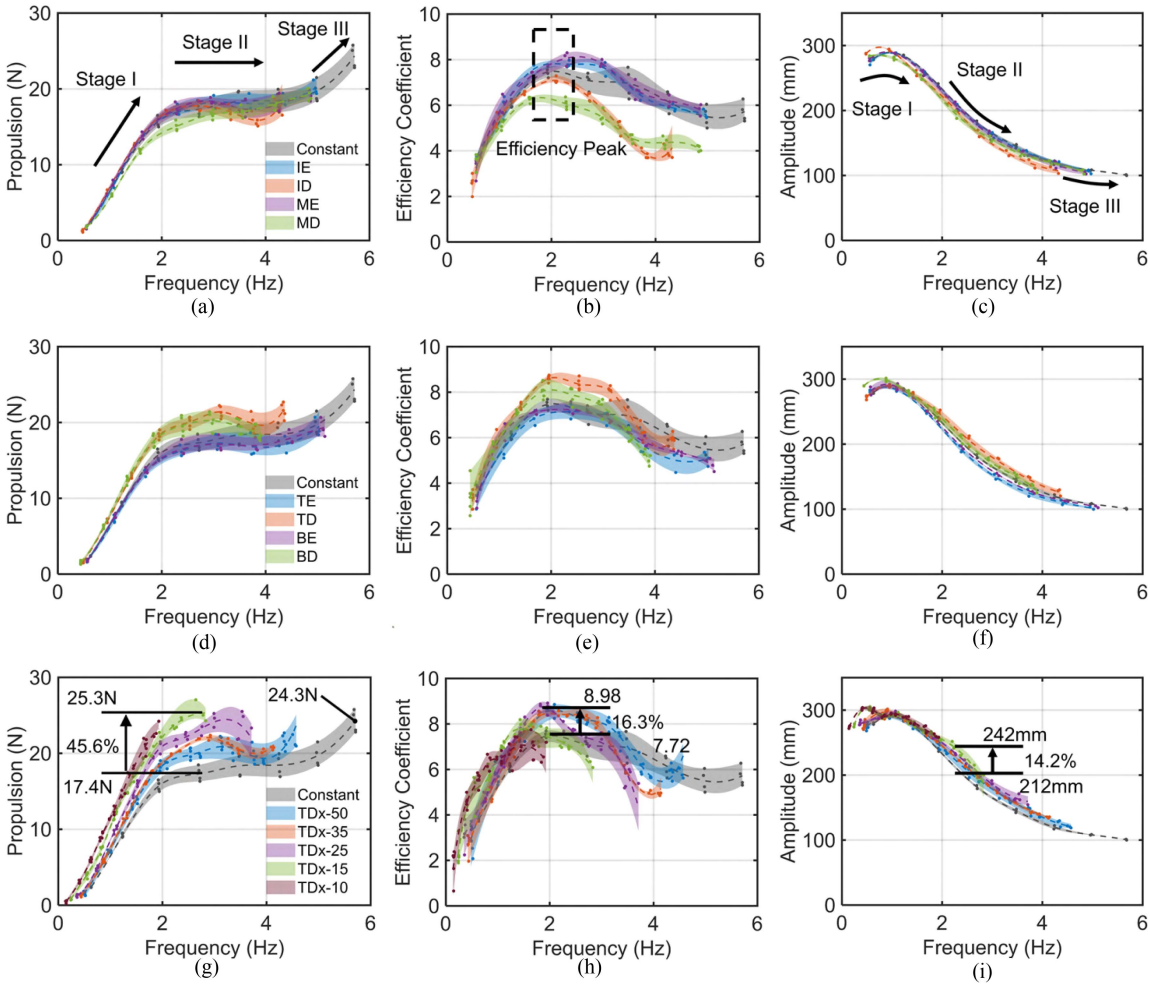

Fig. 13. Experimental results of PAS on propulsion, efficiency coefficient, and amplitude. (a)–(c) Results of the strategies that applied at the initial (IE and ID) and middle (ME and MD) positions of one beat. The propulsion shows a stepwise growing with respect to frequency, while the efficiency coefficient consistently peaking around 2 Hz and the amplitude decrease stepwise with respect to frequency. (d)–(f) Results of strategies applied at the terminal (TE and TD) and bipolar (BE nad BD) of one beat, which broaden the performance envelope of the flexible tail. (g)–(i) Results of the TD strategy employing different decline patterns, demonstrating the maximum enhancement.

TABLE V
METHOD COMPARISON OF ROBOTIC FISH

Studies(Year)	Method	Nominal Thrust-to-Input Ratio (N/Hz/kW)	Controllable Hardware
Gu et al.(2024)	DRL-based Deformation Control	0.037N/2Hz/8.4W=2.2	1 Servo + 2 MFCs
Omari et al.(2022)	Multi-Joint Deformation	0.03N/0.75Hz/14.22W=2.81	3 Servos
Park et al.(2012)	Offline Stiffness Tuning	1.5N/3.21Hz/90W=5.19	1 DC motor
Obayashi et al.(2024)	Hydraulic Stiffness Sequencing	0.19N/0.67Hz/8.7W=31.73	1 Servo + 2 Pumps
DDRFishBot (This work)	Direct-Drive + PAS	**25.3N/2.77Hz/150W=60.89**	1 DC motor

The bold values meant to highlight the value of the current work compared to the other state-of-the-art methods.

strategies, which denotes the relative motion between the tail and water. The gray area is the constant strategy that served as the control group. It can be observed that the total swept area in a cycle increases with frequency, and its fluctuation will gradually flatten out. We calculated the mean and variance of the flapping speed for each cycle to characterize the differences in strength and fluctuation, respectively, as shown in Fig. 17. Based on the analysis of tail-flapping kinematics, the storage and subsequent release of T-EPE during the propulsion generation is verified to achieve performance enhancement. Also, the elastic vibrations of the tail need to be appropriately distributed during oscillations to avoid motion conflict between the peduncle and the tail, which is consistent with the trend shown in the current calculations. Compared to the control group, the TD75-15 has the biggest mean value and variance at each frequency. Due to the redistribution of velocities in the anterior and posterior halves of a single beat, the peak is elevated to an earlier phase of the cycle. The difference between maximum and minimum values

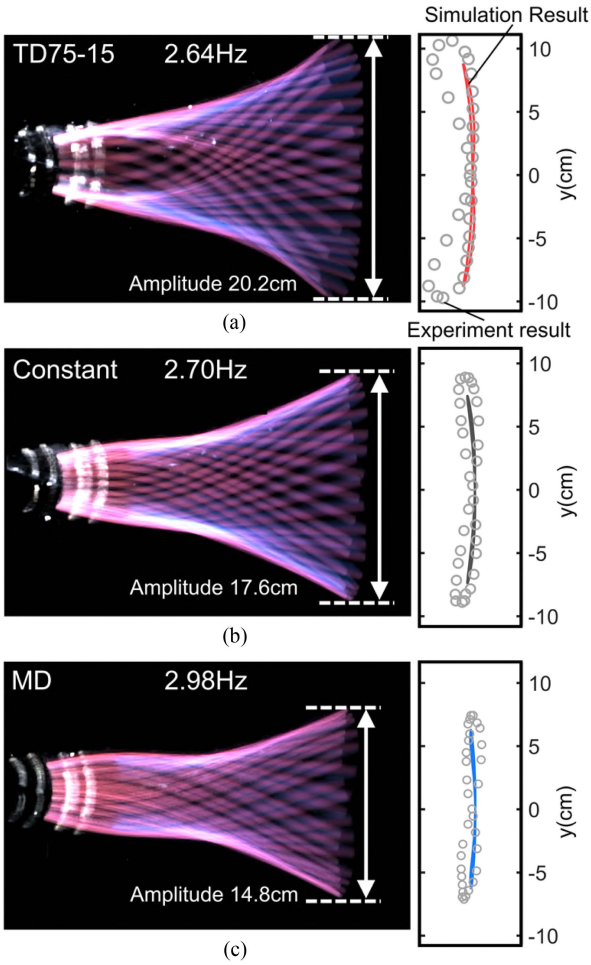

Fig. 14. Deformation pattern of tail-flapping under (a) TD75-15, (b) constant, and (c) MD, respectively, with the comparison of the tip displacement between the experimental and simulation results.

leads to an increase in the variance, indicating an enhanced role of elastic vibration.

Mechanical impedance is used to characterize the impacts of each component in the motion transmission of tail-flapping. The vibration of a flexible tail can be equivalent to a series of mass-spring-damp systems, which is given by

$$m\ddot{y} + c\dot{y} + ky = F(t) \tag{17}$$

where c is the damping coefficient, k is the spring coefficient, and $F(t)$ is the external force input. This equation can be used to obtain the velocity output $\dot{y}$ with the flapping force input $F(t)$ for each section of the tail. Referring to the impedance analysis of a footed robot with compliant component [75], the actuation force is regarded as the input, and the linear velocity of the tail tip is considered as the output. This represents the relationship among the input, the transfer (the compliant element), and the output (the tail tip movment). Then the transfer function representing the impedance of the tail-flapping can be given by

$$H(s) = \frac{1}{ms^2 + cs + k} \tag{18}$$

which characterizes the fundamental vibration characteristics of the peduncle-tail mechanism, including its resonant points. With environmental interaction, the system damping remains constant while the tail vibration is correlated with its inherent compliance. It should be noticed that the generation of different tail-flapping patterns is also related to the peduncle rhythm as the system input. Through this passive compliant transmission component, the rhythmic actuation can easily adjust the manner in which the mechanical power is transmitted to the surrounding water, like playing a musical instrument. In the experiments, the most effective strategy for propulsion generation was to decelerate the tail at the end of each beat. The impedance modeling of tail-flapping can help to reveal the intrinsic mechanism of fish swimming. PAS can alter the rhythmic characteristics of peduncle actuation to reinforce the elastic energy transition. The role of the elastic component of the tail vibration may imply that nonsimple harmonic actuation can achieve an extra excitation effect over the simple harmonic system resonance that reduces the motion conflict between the elastic vibration and the peduncle actuation.

D. Simulated Fluid and Tail Interaction

To enhance the understanding of tail-fluid interactions observed in the experiments, we conducted numerical simulations of tail models using simplified 2-D computational fluid dynamics (CFD) models with equivalent dimensions to the physical counterparts. The simulations were performed using the open-source software OpenFOAM [76]. The positioning of the tail models and the computational domain is illustrated in Fig. 18(a). The computational domain measured 4 m $\times$ 4 m, with far-field boundary conditions applied to replicate an open-water environment. Three grid sizes—0.65 mm, 0.62 mm, and 0.66 mm—corresponding to the constant, MD, and TD configurations, respectively, were employed to generate a grid resolution of 1.07 million cells. Polygonal grids were used to discretize the computational domain.

The tail vortices generated in the wake flows of different tail configurations are shown in Fig. 19, captured over one flapping period on the xy plane. Fish tails transfer more axial momentum to the fluid by generating stronger vortices during propulsive motion [77]. Among the three configurations, the TD75-15 strategy exhibited the strongest vortices in the wake, indicating its superior propulsion generation capability. Furthermore, both the TD75-15 and constant configurations displayed larger tail tip deformation amplitudes, as shown in Fig. 14. This PAS-induced curvature created stronger low-pressure regions, enabling the DDRFishBot to entrain more fluid around the tail and generate stronger shed vortices.

At the moment the tail reverses its direction ($t = 0.5$ T), the entrained fluid rolls off the tail and is released into the wake. As the tail propels, this fluid is shed into the wake, accelerating the flow. Fig. 20 illustrates the flow velocity magnitude within the tail wake. Compared to the constant and MD configurations, the TD75-15 configuration generates higher vorticity and wake velocity, aligning with the experimental findings.

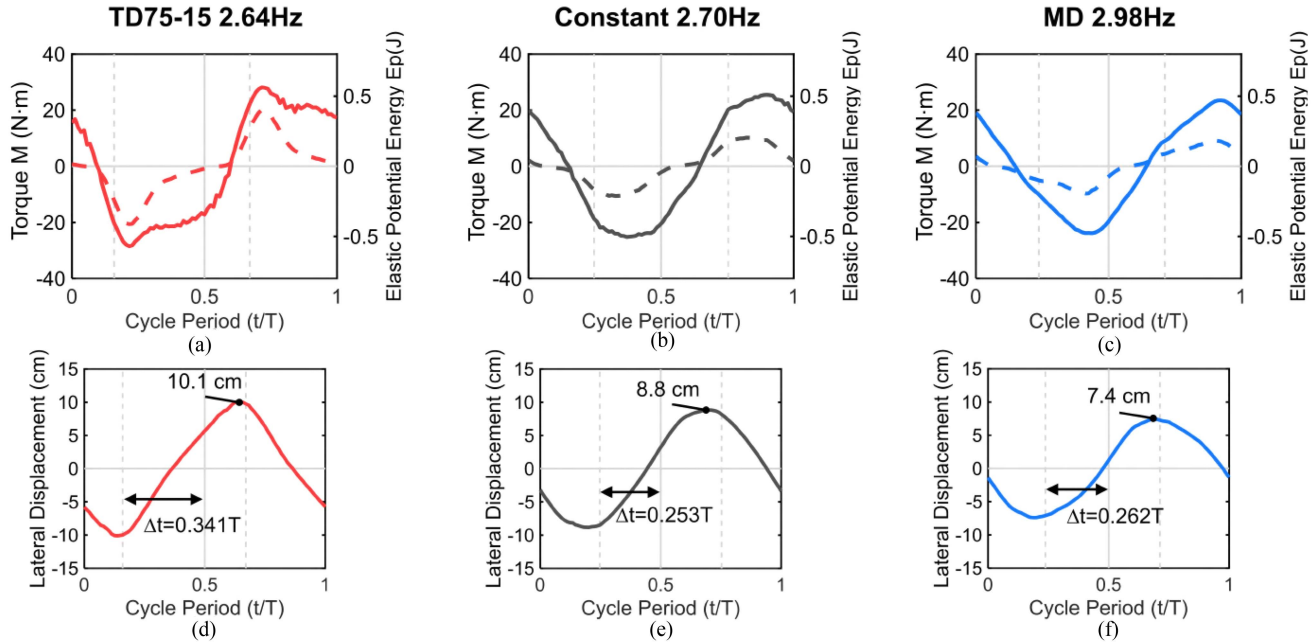

Fig. 15. Experimental results of hydrodynamic torque, T-EPE, and tail tips lateral displacement under: (a) and (d) TD75-15, (b) and (e) constant, and (c) and (f) MD strategies. The elevated release of elastic potential energy (△Ep) signifies increased accumulation and subsequent release of energy, which corresponding to the cooperation between penducle and flexible tail. The prolonged duration (△ t) during the latter half phase of beating enhances the rebound, thereby augmenting the oscillation amplitude.

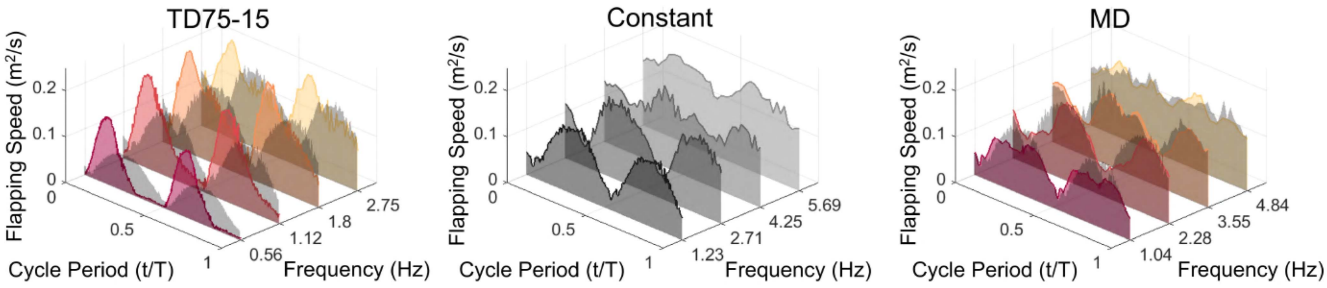

Fig. 16. Statistical evaluation of tail-flapping under (a) TD75-15, (b) constant, and (c) MD. The flapping speed is defined as the area covered by the tail per second.

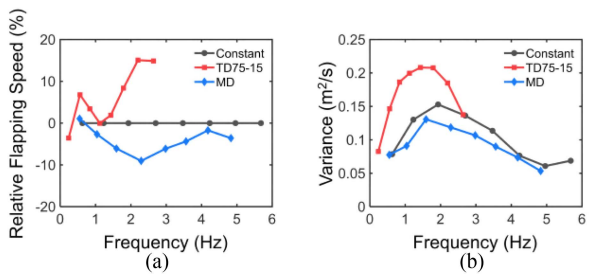

Fig. 17. (a) Percentage change of mean speed and (b) variance of tail-flapping. The variance is defined as the amplitude of flapping speed. Higher values of Var and mean value indicate greater environmental interaction and tail vibration in propulsion, and vice versa.

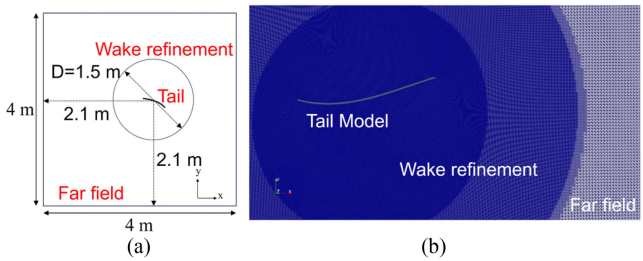

Fig. 18. (a) Computational domain for flapping tail study (not to scale). (b) Corresponding computational grids around the tail.

E. Divergence of Propulsion Performance Exploitation

Since the vibration property is influenced by the tail structure, a further comparison of tail stiffness (K_θ) on the effect of propulsion enhancement is conducted. Fig. 21 presents the tail-flapping pattern with 2 mm and 3 mm PC foil, where the transition of the 2 mm PC foil is more rapid than that of the 3 mm PC foil. Based on the model prediction, this transition caused by the stiffness adjustment can be harnessed to scale the propulsive characteristics, as shown in Fig. 22(a). Connecting the first peak and trough, an envelope about the gait characteristics can be obtained. This envelope denotes the boundary of propulsion

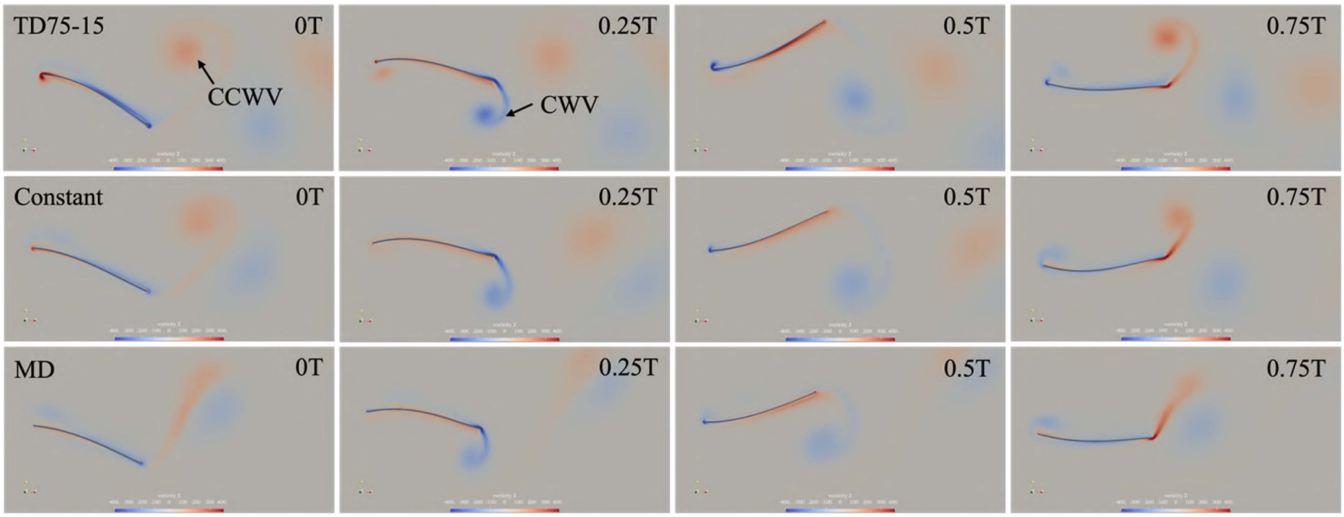

Fig. 19. Tail vortex in the wake flow of tail-flapping under TD75-15, constant, and MD strategies. Contours of streamwise vorticity are presented in the color according to the value of vorticity (1/s). CWV and CCWV indicate clock-wise and counter clock-wise vortex. T denotes one period of flapping motion.

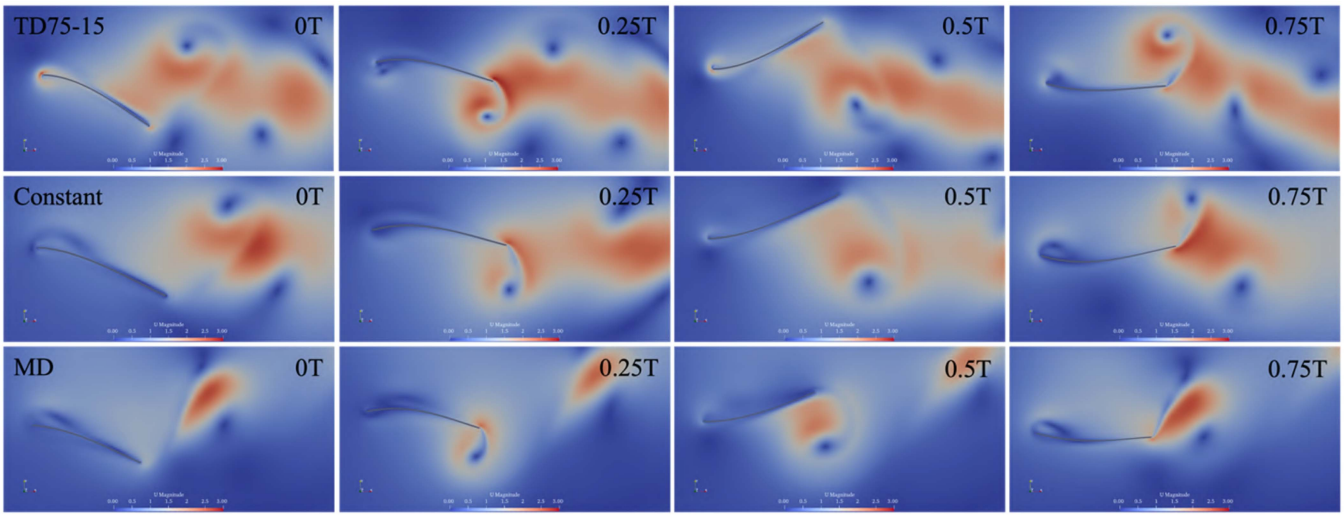

Fig. 20. Flow velocity in the wake flow of tail-flapping under TD75-15, constant, and MD strategies. Contours of flow velocity are presented in the color according to the velocity magnitude (m/s). T denotes one period of flapping motion.

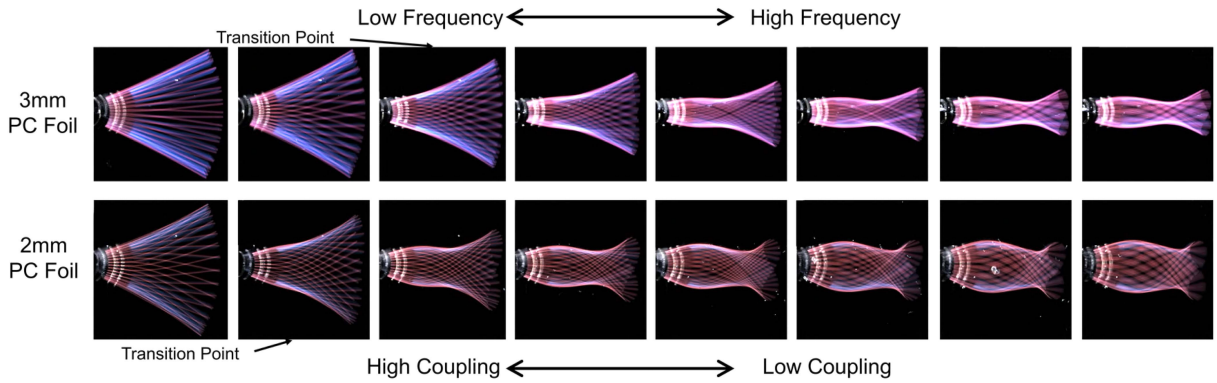

Fig. 21. Transition period of the tail-flapping coupling. The flared shape at lower frequencies indicates high coupling, while the spindle-like shape at higher frequencies indicates low coupling. The transition of 2 mm PC foil (low stiffness) occurs at a lower frequency and proceeds more rapidly than 3 mm PC foil (high stiffness).

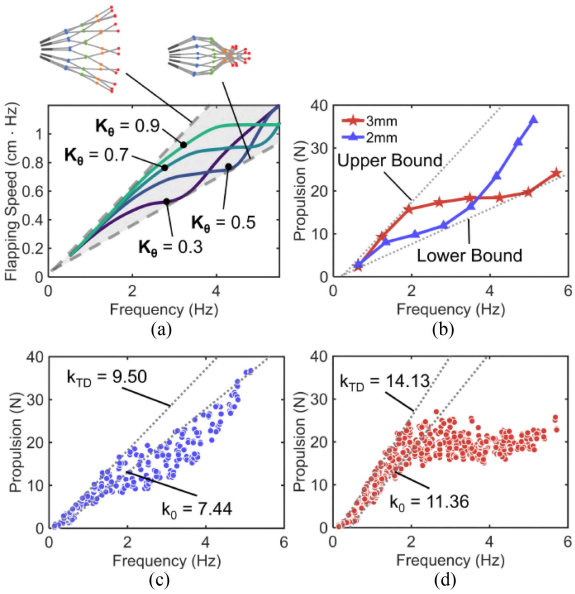

Fig. 22. Exploitation of propulsion performance divergence. (a) Prediction of propulsive characteristics under tail stiffness (K_θ) change. (b) Experimental result of propulsion performance with 2 mm and 3 mm PC foil. The PAS are validated on the (c) 2 mm and (d) 3 mm PC foil. The slope of propulsion generation for TD strategy (k_{TD}) exceeds that of constant strategy (k_0) across both foil.

generation through tail-flapping. As the stiffness changes, the propeller can be scaled to the desired gait within the boundary of two tail-flapping patterns.

This principle is validated through comparative testing as shown in Fig. 22(b), where the tail configuration from Fig. 12 is substituted by a 2 mm PC foil. The propulsion increases rapidly with frequency until 1.3 Hz and then enters a shorter plateau before secondary rapid rising near 3.5 Hz. The results show a similar trend as the model predicted. There is a decrease in the onset frequency of transitions and a shorter plateau period. This is in agreement with the collaborative relationship between the elastic and damping components indicated by (18). Limited by the internal elastic restoration force, the T-EPE for the 2 mm tail to utilize is less than the 3 mm tail. While the propulsion enhancement from the rhythmic coupling effect primarily relies on the amplitude increment and elastic energy circulation. After 3.5 Hz, the 2 mm PC foil has already passed the lower boundary of low-coupling when the propulsion generation is mainly contributed by the frequency increment. As for the prototype tested in this article, the tradeoff between the amplitude and frequency of the 2 mm tail alleviates the propulsion enhancement so that it is not sufficient to fill the gap compared to the maximal power state. However, the PAS still presents a propulsion enhancement with an optimal 45% increment in the slope of propulsion generation by TD75-25 strategy, compared to the 27.7% in 2 mm PC foil, as shown in Fig. 22(c) and (d).

F. PSO-Based Formulation of PAS

Previously, we have parametrically explored the PAS on a direct-drive system in model predictions and prototype experiments, demonstrating the effect of reallocated power intensity

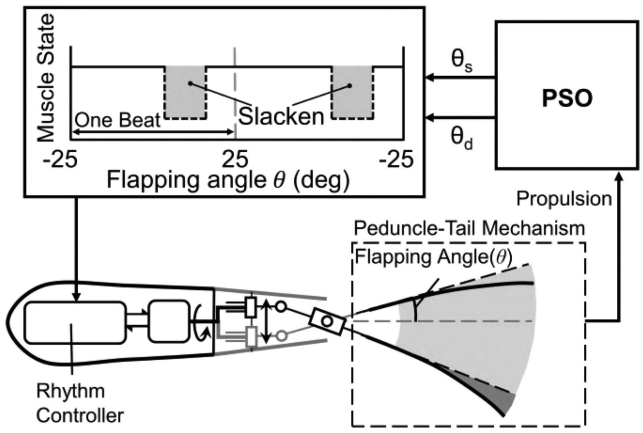

Fig. 23. Scheme of strategy optimization for power allocation based on PSO algorithm.

and position on the tail rebound behavior as well as the enhancement of propulsive performance. To demonstrate the effectiveness of this bioinspired approach and expand its applicability, we employed a particle swarm optimization (PSO) algorithm to find the targeted rhythmic patterns that maximize and minimize propulsion force as shown in Fig. 23. The PSO algorithm performs iterative optimization in a multidimensional space. Particles update their positions p_i and velocities v_i according to the following equations:

$$\begin{cases} v_i(n+1) = c_0 \times v_i(n) + c_1 \times \text{rand} \times (p_{bi}(n) - p_i(n)) \\ \qquad\qquad + c_2 \times \text{rand} \times (g_b(n) - p_i(n)) \\ p_i(n+1) = p_i(n) + v_i(n+1) \end{cases}, \tag{19}$$

where n denotes the number of iterations, c_0 is the inertia weight, c_1 and c_2 are the learning factors, rand is a random number in the range of [0,1], p_{bi} is the individual extremum of each particle, g_b is the global extremum and the output of the algorithm. The position space of the particles is formed by θ_s and θ_d, which represents the start timing and the duration of slack within a cycle, respectively, and is constrained by

$$0 \le \theta_s \le B, \theta_s + \theta_d \le B. \tag{20}$$

Setting $S_a = 100\%$, the slackness level S_s is bounded by

$$\theta_d / B \times S_s = 12.5\%, 10\% \le S_s \le 90\%. \tag{21}$$

The fitness function for maximizing propulsion is defined as

$$g = -(\overline{P}_{\text{pso}} - \overline{P}_{\text{constant}})/\overline{P}_{\text{constant}} \tag{22}$$

whereas the fitness function for minimizing propulsion is defined as

$$g = (\overline{P}_{\text{pso}} - \overline{P}_{\text{constant}})/\overline{P}_{\text{constant}}. \tag{23}$$

Here, $\overline{P}_{\text{constant}}$ represents the propulsion without the applying rhythmic pattern, $\overline{P}_{\text{pso}}$ is the propulsion using the rhythmic pattern determined by θ_s and θ_d. With the parameters set as shown in Table VI, the PSO algorithm minimizes the value of g to find the targeted rhythmic pattern.

TABLE VI
PARAMETERS OF THE PSO

parameter	value
particles number	15
Inertia weight c_0	0.7
Personal learning factor c_1	1.4
Social learning factor c_2	1.4

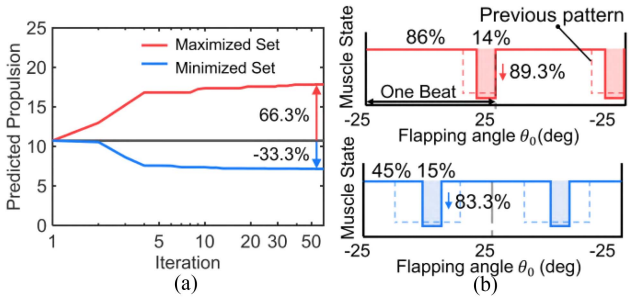

Fig. 24. (a) Predicted propulsion curves during PSO progression. (b) Targeted rhythm under the fitness function for maximal and minimal propulsion.

The predicted propulsion in both targets converged after 50 iterations as shown in Fig. 24(a), achieving a flexible propulsion performance regulation with a 66.3% increase and a 33.3% decrease. The optimized PAS is shown in Fig. 24(b), which is consistent with our previous bioinspired strategy, located at the terminal and middle, respectively, which demonstrates the effectiveness and scalibility of the proposed PAS method.

V. CONCLUSION

In this article, we proposed a PAS of tail-flapping, which regulates the power input of the motor in the flapping cycle, aiming to enhance the propulsion by emulating the rhythmic regulation of biological muscles. A robotic fish prototype, DDRFishBot, is developed to investigate the effect of the PAS on propulsion enhancement, which has the following two main advantages.

1) Achieving leading NTIR of 60.98 (N/Hz/kW) on the DDRFishBot using only its inherent structural compliance, without additional mechanisms for deformation or stiffness tuning.
2) Enlarging the controllable space of propulsion performance by exploiting the inherent flexibility of the tail through the rhythmic coupling effect on the peduncle-tail mechanism.

The PRBM is derived to describ the deformation pattern of the peduncle-tail mechanism under different flapping strategies. The EBT-based propulsion estimation verifies that the PAS can enhance propulsion by utilizing the T-EPE. By adjusting the power allocation of the peduncle actuation, the accumulation of T-EPE can be enhanced during the anterior of each flapping beat. This can prolong the tail rebound, resulting in a flared tail envelope with larger amplitude and increased propulsion. The experimental results demonstrate that the allocation pattern of PAS can modulate the storage and release of T-EPE within a considerable range, thereby flexibly regulating the tail rebound. Further CFD analysis enhances the understanding of tail-fluid interaction that this tail rebound behavior enables the DDRFish-Bot to entrain more fluid around the tail and generate stronger shed vortices.

Combining model prediction and experimental validation, the DDRFishBot was verified to actively utilize the inherent flexibility of the tail. Compared to the maximal power state by constant strategy, the slope of propulsion generation is enhanced by 124%, with a 53.5% reduction in frequency requirement for the peak propulsion, which indicates a more effective mechanical power transmission for tail-flapping. Within the expanded performance space, the PAS generate a 228% increase in T-EPE release, resulting in a 36% enhancement in amplitude, 45.6% increase in propulsion, and 16.3% in efficiency coefficient. Further kinematic analysis reveals the mechanism of the optimal TD strategy among the tested group. Statistical evaluation reveals a correlation between the propulsion enhancement effect and two parameters, namely relative velocity and variance that, respectively, describe the average strength and fluctuation of tail-flapping.

Simply connected to passive flexible tails with different stiffnesses, the motor with a scotch yoke mechanism can exhibit similar propulsion enhancement based on the proposed PAS. Numerical optimization of PAS was also implemented based on the PSO algorithm to achieve the formulation of rhythm patterns. These show the potential of applying the proposed PAS to other underwater robotic fish that possess similar actuation and flexible tail mechanisms.

Currently, the voltage regulation of PAS compromises maximum power output, while the inherent mechanical limitations of scotch yoke mechanisms constrain power transmission efficiency, which will be the focus of our future work. Our research will persist in investigating the intrinsic mechanisms of fish swimming, and further exploring the inherent potential of the subcomponents for the overall propulsion performance of robots.

ACKNOWLEDGMENT

The authors would like to thank Mr. Zhang Zhicheng for CFD calculation.

REFERENCES

[1] X. Tan, "Autonomous robotic fish as mobile sensor platforms: Challenges and potential solutions," *Mar. Technol. Soc. J.*, vol. 45, no. 4, pp. 31–40, 2011.
[2] M. Sfakiotakis, D. M. Lane, and J. B. C. Davies, "Review of fish swimming modes for aquatic locomotion," *IEEE J. Ocean. Eng.*, vol. 24, no. 2, pp. 237–252, Apr. 1999.
[3] J. Delmerico et al., "The current state and future outlook of rescue robotics," *J. Field Robot.*, vol. 36, no. 7, pp. 1171–1191, 2019.
[4] M. S. Triantafyllou and G. S. Triantafyllou, "An efficient swimming machine," *Sci. Amer.*, vol. 272, no. 3, pp. 64–70, 1995.
[5] J. Yuh, "Design and control of autonomous underwater robots: A survey," *Auton. Robots*, vol. 8, pp. 7–24, 2000.
[6] P. Duraisamy, R. K. Sidharthan, and M. N. Santhanakrishnan, "Design, modeling, and control of biomimetic fish robot: A review," *J. Bionic Eng.*, vol. 16, pp. 967–993, 2019.

[7] G. V. Lauder, E. J. Anderson, J. Tangorra, and P. G. Madden, "Fish biorobotics: Kinematics and hydrodynamics of self-propulsion," *J. Exp. Biol.*, vol. 210, no. 16, pp. 2767–2780, 2007.

[8] R. W. Blake, "Fish functional design and swimming performance," *J. Fish Biol.*, vol. 65, no. 5, pp. 1193–1222, 2004.

[9] A. Raj and A. Thakur, "Fish-inspired robots: Design, sensing, actuation, and autonomy—A review of research," *Bioinspiration Biomimetics*, vol. 11, no. 3, 2016, Art. no. 031001.

[10] D. Scaradozzi, G. Palmieri, D. Costa, and A. Pinelli, "BCF swimming locomotion for autonomous underwater robots: A review and a novel solution to improve control and efficiency," *Ocean Eng.*, vol. 130, pp. 437–453, 2017.

[11] V. Di Santo et al., "Convergence of undulatory swimming kinematics across a diversity of fishes," *Proc. Nat. Acad. Sci.*, vol. 118, no. 49, 2021, Art. no. e2113206118.

[12] Y. Liu and H. Jiang, "Research development on fish swimming," *Chin. J. Mech. Eng.*, vol. 35, no. 1, 2022, Art. no. 114.

[13] T. Y. Wu, "Fish swimming and bird/insect flight," *Annu. Rev. Fluid Mechan.*, vol. 43, pp. 25–58, 2011.

[14] M. Lighthill, "Note on the swimming of slender fish," *J. Fluid Mechan.*, vol. 9, no. 2, pp. 305–317, 1960.

[15] F. Xie, Z. Li, Y. Ding, Y. Zhong, and R. Du, "An experimental study on the fish body flapping patterns by using a biomimetic robot fish," *IEEE Robot. Automat. Lett.*, vol. 5, no. 1, pp. 64–71, Jan. 2020.

[16] M. Kaya and I. H. Tuncer, "Nonsinusoidal path optimization of a flapping airfoil," *AIAA J.*, vol. 45, no. 8, pp. 2075–2082, 2007.

[17] K. Lu, Y. Xie, and D. Zhang, "Numerical study of large amplitude, nonsinusoidal motion and camber effects on pitching airfoil propulsion," *J. Fluids Struct.*, vol. 36, pp. 184–194, 2013.

[18] T. Y.-T. Wu, "Hydromechanics of swimming propulsion. Part 1. swimming of a two-dimensional flexible plate at variable forward speeds in an inviscid fluid," *J. Fluid Mechan.*, vol. 46, no. 2, pp. 337–355, 1971.

[19] K. N. Lucas, P. J. Thornycroft, B. J. Gemmell, S. P. Colin, J. H. Costello, and G. V. Lauder, "Effects of non-uniform stiffness on the swimming performance of a passively-flexing, fish-like foil model," *Bioinspiration Biomimetics*, vol. 10, no. 5, 2015, Art. no. 056019.

[20] Y. Zhong, Z. Hong, Y. Li, and J. Yu, "A general kinematic model of fish locomotion enables robot fish to master multiple swimming motions," *IEEE Trans. Robot.*, vol. 40, pp. 750–763, 2024.

[21] J. C. Liao, "A review of fish swimming mechanics and behaviour in altered flows," *Philos. Trans. Roy. Soc. B: Biol. Sci.*, vol. 362, no. 1487, pp. 1973–1993, 2007.

[22] Y. Pan and G. V. Lauder, "Combining computational fluid dynamics and experimental data to understand fish schooling behavior," *Integrative Comp. Biol.*, vol. 64, no. 3, pp. 753–768, 2024.

[23] G. Li, U. K. Müller, J. L. van Leeuwen, and H. Liu, "Body dynamics and hydrodynamics of swimming fish larvae: A computational study," *J. Exp. Biol.*, vol. 215, no. 22, pp. 4015–4033, 2012.

[24] L. Li, M. Nagy, J. M. Graving, J. Bak-Coleman, G. Xie, and I. D. Couzin, "Vortex phase matching as a strategy for schooling in robots and in fish," *Nature Commun.*, vol. 11, no. 1, 2020, Art. no. 5408.

[25] X. Wu, X. Zhang, X. Tian, X. Li, and W. Lu, "A review on fluid dynamics of flapping foils," *Ocean Eng.*, vol. 195, 2020, Art. no. 106712.

[26] Y.-J. Park, U. Jeong, J. Lee, S.-R. Kwon, H.-Y. Kim, and K.-J. Cho, "Kinematic condition for maximizing the thrust of a robotic fish using a compliant caudal fin," *IEEE Trans. Robot.*, vol. 28, no. 6, pp. 1216–1227, Dec. 2012.

[27] T. Wang, Z. Ren, W. Hu, M. Li, and M. Sitti, "Effect of body stiffness distribution on larval fish-like efficient undulatory swimming," *Sci. Adv.*, vol. 7, no. 19, 2021, Art. no. eabf7364.

[28] U. K. Müller and J. L. Van Leeuwen, "Undulatory fish swimming: From muscles to flow," *Fish Fisheries*, vol. 7, no. 2, pp. 84–103, 2006.

[29] M. W. Westneat, W. Hoese, C. A. Pell, and S. A. Wainwright, "The horizontal septum: Mechanisms of force transfer in locomotion of scombrid fishes (scombridae, perciformes)," *J. Morphol.*, vol. 217, no. 2, pp. 183–204, 1993.

[30] C. Wardle, J. Videler, and J. Altringham, "Tuning in to fish swimming waves: Body form, swimming mode and muscle function," *J. Exp. Biol.*, vol. 198, no. 8, pp. 1629–1636, 1995.

[31] E. D. Tytell, C.-Y. Hsu, and L. J. Fauci, "The role of mechanical resonance in the neural control of swimming in fishes," *Zool.*, vol. 117, no. 1, pp. 48–56, 2014.

[32] J. Chen, W. Friesen, and T. Iwasaki, "Mechanisms underlying rhythmic locomotion: Body–fluid interaction in undulatory swimming," *J. Exp. Biol.*, vol. 214, no. 4, pp. 561–574, 2011.

[33] J. Chen, W. O. Friesen, and T. Iwasaki, "Mechanisms underlying rhythmic locomotion: Interactions between activation, tension and body curvature waves," *J. Exp. Biol.*, vol. 215, no. 2, pp. 211–219, 2012.

[34] N. Gravish and G. V. Lauder, "Robotics-inspired biology," *J. Exp. Biol.*, vol. 221, no. 7, 2018, Art. no. jeb138438.

[35] J. Yu, M. Wang, H. Dong, Y. Zhang, and Z. Wu, "Motion control and motion coordination of bionic robotic fish: A review," *J. Bionic Eng.*, vol. 15, pp. 579–598, 2018.

[36] J. D. Altringham and D. J. Ellerby, "Fish swimming: Patterns in muscle function," *J. Exp. Biol.*, vol. 202, no. 23, pp. 3397–3403, 1999.

[37] J. Han et al., "Undulatory motion of sailfish-like robot via a new single-degree-of-freedom modularized spatial mechanism," *Mechanism Mach. Theory*, vol. 191, 2024, Art. no. 105502.

[38] D. Rus and M. T. Tolley, "Design, fabrication and control of soft robots," *Nature*, vol. 521, no. 7553, pp. 467–475, 2015.

[39] L. C. Rome, D. Swank, and D. Corda, "How fish power swimming," *Science*, vol. 261, no. 5119, pp. 340–343, 1993.

[40] R. L. Marsh, "How muscles deal with real-world loads: The influence of length trajectory on muscle performance," *J. Exp. Biol.*, vol. 202, no. 23, pp. 3377–3385, 1999.

[41] G. V. Lauder, B. Flammang, and S. Alben, "Passive robotic models of propulsion by the bodies and caudal fins of fish," *Integrative and Comparative Biology*, vol. 52, no. 5, pp. 576–587, 2012, doi: 10.1093/icb/ics096.

[42] S. A. Burden, T. Libby, K. Jayaram, S. Sponberg, and J. M. Donelan, "Why animals can outrun robots," *Sci. Robot.*, vol. 9, no. 89, 2024, Art. no. eadi9754.

[43] B. Webb, "Can robots make good models of biological behaviour?," *Behav. Brain Sci.*, vol. 24, no. 6, pp. 1033–1050, 2001.

[44] Y. Zhong, Z. Li, and R. Du, "A novel robot fish with wire-driven active body and compliant tail," *IEEE/ASME Trans. Mechatron.*, vol. 22, no. 4, pp. 1633–1643, Aug. 2017.

[45] Z. Yu et al., "Cooperative motion mechanism of a bionic sailfish robot with high motion performance," *IEEE Robot. Autom. Lett.*, vol. 9, no. 7, pp. 6592–6599, Jul. 2024.

[46] S. B. Behbahani and X. Tan, "Design and modeling of flexible passive rowing joint for robotic fish pectoral fins," *IEEE Trans. Robot.*, vol. 32, no. 5, pp. 1119–1132, Oct. 2016.

[47] A. Jusufi, D. M. Vogt, R. J. Wood, and G. V. Lauder, "Undulatory swimming performance and body stiffness modulation in a soft robotic fish-inspired physical model," *Soft Robot.*, vol. 4, no. 3, pp. 202–210, 2017.

[48] Y. Wang et al., "A biorobotic adhesive disc for underwater hitchhiking inspired by the remora suckerfish," *Sci. Robot.*, vol. 2, no. 10, 2017, Art. no. eaan8072.

[49] B. Chen and H. Jiang, "Body stiffness variation of a tensegrity robotic fish using antagonistic stiffness in a kinematically singular configuration," *IEEE Trans. Robot.*, vol. 37, no. 5, pp. 1712–1727, Oct. 2021.

[50] J. Wang and X. Tan, "Averaging tail-actuated robotic fish dynamics through force and moment scaling," *IEEE Trans. Robot.*, vol. 31, no. 4, pp. 906–917, Aug. 2015.

[51] X. Ma, G. Wang, and K. Liu, "Design and optimization of a multimode amphibious robot with propeller-leg," *IEEE Trans. Robot.*, vol. 38, no. 6, pp. 3807–3820, Dec. 2022.

[52] F. Berlinger, M. Gauci, and R. Nagpal, "Implicit coordination for 3D underwater collective behaviors in a fish-inspired robot swarm," *Sci. Robot.*, vol. 6, no. 50, 2021, Art. no. eabd8668.

[53] S. Liu, C. Liu, Y. Liang, L. Ren, and L. Ren, "Tunable stiffness caudal peduncle leads to higher swimming speed without extra energy," *IEEE Robot. Autom. Lett.*, vol. 8, no. 9, pp. 5886–5893, Sep. 2023.

[54] Z. Wolf, A. Jusufi, D. Vogt, and G. Lauder, "Fish-like aquatic propulsion studied using a pneumatically-actuated soft-robotic model," *Bioinspiration Biomimetics*, vol. 15, no. 4, 2020, Art. no. 046008.

[55] C. J. Esposito, J. L. Tangorra, B. E. Flammang, and G. V. Lauder, "A robotic fish caudal fin: Effects of stiffness and motor program on locomotor performance," *J. Exp. Biol.*, vol. 215, no. 1, pp. 56–67, 2012.

[56] T. Bujard, F. Giorgio-Serchi, and G. D. Weymouth, "A resonant squid-inspired robot unlocks biological propulsive efficiency," *Sci. Robot.*, vol. 6, no. 50, 2021, Art. no. eabd2971.

[57] Q. Zhong et al., "Tunable stiffness enables fast and efficient swimming in fish-like robots," *Sci. Robot.*, vol. 6, no. 57, 2021, Art. no. eabe4088.

[58] J. Zhu et al., "Tuna robotics: A high-frequency experimental platform exploring the performance space of swimming fishes," *Sci. Robot.*, vol. 4, no. 34, 2019, Art. no. eaax4615.

[59] R. Thandiackal et al., "Emergence of robust self-organized undulatory swimming based on local hydrodynamic force sensing," *Sci. Robot.*, vol. 6, no. 57, 2021, Art. no. eabf6354.

[60] R. Zhang, Z. Shen, and Z. Wang, "Ostraciiform underwater robot with segmented caudal fin," *IEEE Robot. Autom. Lett.*, vol. 3, no. 4, pp. 2902–2909, Oct. 2018.
[61] R. Zhang, Z. Shen, H. Zhong, J. Tan, Y. Hu, and Z. Wang, "A cephalopod-inspired soft-robotic siphon for thrust vectoring and flow rate regulation," *Soft Robot.*, vol. 8, no. 4, pp. 416–431, 2021.
[62] Z. Shen, J. Na, and Z. Wang, "A biomimetic underwater soft robot inspired by cephalopod mollusc," *IEEE Robot. Autom. Lett.*, vol. 2, no. 4, pp. 2217–2223, Oct. 2017.
[63] H. Zhong, Z. Shen, Y. Zhao, K. Tang, W. Wang, and Z. Wang, "A hybrid underwater manipulator system with intuitive muscle-level SEMG mapping control," *IEEE Robot. Autom. Lett.*, vol. 5, no. 2, pp. 3198–3205, Apr. 2020.
[64] "Fastest 50 m swim by a robotic fish," *Guinness World Rec.*, [Online]. Available: https://www.guinnessworldrecords.com/world-records/413784-fastest-50-metres-by-a-robotic-fish (accessed: citation>Jun. 18, 2025).
[65] J. Altringham, C. Wardle, and C. Smith, "Myotomal muscle function at different locations in the body of a swimming fish," *J. Exp. Biol.*, vol. 182, no. 1, pp. 191–206, 1993.
[66] H.-J. Su, "A pseudorigid-body 3R model for determining large deflection of cantilever beams subject to tip loads," *J. Mechanisms Robot.*, vol. 1, no. 2, 2009, Art. no. 021008.
[67] L. L. Howell, "Compliant mechanisms," in *Proc. 21st Century Kinematics: 2012 NSF Workshop*, 2013, pp. 189–216.
[68] J. D. Altringham and I. A. Johnston, "Scaling effects on muscle function: Power output of isolated fish muscle fibres performing oscillatory work," *J. Exp. Biol.*, vol. 151, no. 1, pp. 453–467, 1990.
[69] F. Lou, N. Curtin, and R. Woledge, "Elastic energy storage and release in white muscle from dogfish scyliorhinus canicula," *J. Exp. Biol.*, vol. 202, no. 2, pp. 135–142, 1999.
[70] J. D. Altringham and I. A. Johnston, "Modelling muscle power output in a swimming fish," *J. Exp. Biol.*, vol. 148, no. 1, pp. 395–402, 1990.
[71] R. M. Shelton, P. J. Thornycroft, and G. V. Lauder, "Undulatory locomotion of flexible foils as biomimetic models for understanding fish propulsion," *J. Exp. Biol.*, vol. 217, no. 12, pp. 2110–2120, 2014.
[72] M. Omari, M. Ghommem, L. Romdhane, and M. R. Hajj, "Performance analysis of bio-inspired transformable robotic fish tail," *Ocean Eng.*, vol. 244, 2022, Art. no. 110406.
[73] J. Gu, J. Wang, Z. Liu, M. Tan, J. Yu, and Z. Wu, "Deformation control and thrust analysis of a flexible fishtail with muscle-like actuation," *IEEE Trans. Robot.*, vol. 41, pp. 159–179, 2025.
[74] N. Obayashi, K. Junge, P. Singh, and J. Hughes, "Online hydraulic stiffness modulation of a soft robotic fish tail for improved thrust and efficiency," *Soft Robot.*, vol. 12, no. 2, pp. 242–252, 2025.
[75] T. Boaventura, J. Buchli, C. Semini, and D. G. Caldwell, "Model-based hydraulic impedance control for dynamic robots," *IEEE Trans. Robot.*, vol. 31, no. 6, pp. 1324–1336, Dec. 2015.
[76] H. Jasak et al., "Openfoam: A c library for complex physics simulations," in *Proc. Int. Workshop Coupled Methods Numer. Dyn.*, Dubrovnik, Croatia, 2007, vol. 1000, pp. 1–20.
[77] O. Akanyeti, J. Putney, Y. R. Yanagitsuru, G. V. Lauder, W. J. Stewart, and J. C. Liao, "Accelerating fishes increase propulsive efficiency by modulating vortex ring geometry," *Proc. Nat. Acad. Sci.*, vol. 114, no. 52, pp. 13828–13833, 2017.

Biao Wu (Student Member, IEEE) received the B.E. degree in robotics engineering in 2021 from the Southern University of Science and Technology, Shenzhen, China, where he is currently working toward the M.Sc. degree in electronic science and technology with the Department of Mechanical and Energy Engineering.

His research interest includes biomimetic and soft robotics.

Chaoyi Huang (Student Member, IEEE) received the B.E. degree in mechanical design, manufacturing, and automation in 2019 from Central South University, Changsha, China, and the M.Sc. degree in mechanical engineering in 2020 from the University of Hong Kong, Hong Kong, where he is currently working toward the Ph.D. degree in mechanical engineering.

His research interests include soft robots and bionic robots.

Xiangru Li (Student Member, IEEE) received the B.Eng. (Hons.) degree in mechanical engineering in 2020 from the University of Hong Kong, Hong Kong, and the M.S. degree in mechanical engineering in 2022 from the Hong Kong University of Science and Technology, Hong Kong, where he is currently working toward the Ph.D. degree in mechanical and aerodynamics engineering.

His research interest includes underwater bionic robotics and aerodynamics and physiology in sports science.

Jiahao Xu (Student Member, IEEE) received the B.Eng. degree in mechanical design manufacturing and automation from the Guangdong University of Technology, Guangzhou, China, in 2021. He is currently working toward the M.Sc. degree in intelligent manufacturing and robotics with the Department of Mechanical Engineering and Energy Engineering, Southern University of Science and Technology, Shenzhen, China.

His research interests include actuating and perception for soft robotics.

Sicong Liu (Member, IEEE) received the B.S. (Hons.) degree in mechanical design manufacturing and automation and the M.S. degree in mechanical design and theory from the Harbin Institute of Technology (HIT), Harbin, China, in 2009 and 2011, respectively, and the Ph.D. degree in robotics and engineering mechanics from Nanyang Technological University, Singapore, in 2015.

In 2016, he was a Postdoctoral Research Fellow with Nanyang Technological University, Singapore. He was a Mechanical Engineer with the DJI, in 2017. Then, he was a Senior Mechanical Engineer with UBTECH, Shenzhen, China, in 2019. He was a Research Associate Professor with the Southern University of Science and Technology, Shenzhen, China, in 2024. He is currently an Associate Professor with the Sino-German College of Intelligent Manufacturing, Shenzhen Technology University, Shenzhen. His research interest includes deployable structures inspired by origami, soft robotics and biorobotics.

James Lam (Fellow, IEEE) received the B.Sc. (1st Hons.) degree in mechanical engineering from the University of Manchester, Manchester, U.K., and the M.Phil. and Ph.D. degrees from the University of Cambridge, Cambridge, U.K.

He is currently a Chair Professor of Control Engineering with the University of Hong Kong, Hong Kong, where he joined in 1993. Before that, he held faculty positions with the City University of Hong Kong, Hong Kong, and the University of Melbourne, Melbourne, VIC, Australia. He is a Croucher Scholar, Croucher Fellow, Distinguished Visiting Fellow of the Royal Academy of Engineering, and Cheung Kong Chair Professor. He holds many professional designations, including Chartered Mathematician (CMath), Chartered Scientist (CSci), Chartered Engineer (CEng).

Dr. Lam is currently a Fellow of several prestigious institutions such as the Institute of Electrical and Electronic Engineers (FIEEE), Institution of Engineering and Technology (FIET), Institute of Mathematics and Its Applications (FIMA), Institution of Mechanical Engineers (FIMechE), Hong Kong Institution of Engineers (FHKIE), Asia-Pacific Artificial Intelligence Association (FAAIA), and a Distinguished Fellow of International Engineering and Technology Institute (DFIETI). He is also an Editor-in-Chief for *IET Control Theory and Applications*, *Journal of The Franklin Institute*, *Proc. IMechE Part I: Journal of Systems and Control Engineering*, *Franklin Open*, and *IET Journal of Engineering*. He has also held editorial positions in journals such as the *Journal of Sound and Vibration*, *Asian Journal of Control*, *Cogent Engineering*, *International Journal of Systems Science*, *Automatica*, and *Multidimensional Systems and Signal Processing*. His research contributions have been recognized through his inclusion as a Highly Cited Researcher in Engineering/Computer Science/Cross-Fields. His WoS H-index is 106, and Scopus H-index is 111. He is currently an elected Foreign Member of *Academia Europaea* and an Academician of the *International Academy of Systems and Cybernetic Sciences*.

Zheng Wang (Senior Member, IEEE) received the B.Sc. degree (Hons.) in automatic control from Tsinghua University, Beijing, China, in 2004, the M.Sc. degree (Hons.) in control systems from the Imperial College London, London. U.K., in 2005, and the Ph.D. degree (Hons.) in electrical engineering from Technische Universitaet Muenchen, Munich, Germany, in 2010.

He was a Postdoctoral Research Fellow with Nanyang Technological University, Singapore, from 2010 to 2013, and a Postdoctoral Fellow with the School of Engineering and Applied Sciences and the Wyss Institute of Bioinspired Engineering, Harvard University, Cambridge, MA, USA, in 2013 and 2014, respectively. Since July 2014, he has been an Assistant Professor with the Department of Mechanical Engineering, The University of Hong Kong, Hong Kong. He has been a Professor of Robotics with the Department of Mechanical and Energy Engineering, Southern University of Science and Technology, Shenzhen, China, since February 2019.

Jiansheng Dai (Fellow, IEEE) received the B.Sc. and M.Sc. degrees from Shanghai Jiao Tong University, Shanghai, China, and the Ph.D. degree in advanced kinematics and robotics from the University of Salford, Salford, U.K., in 1993.

He has authored or coauthored more than 700 peer-reviewed papers, and nine authored books, he has graduated more than 100 Ph.D. students and Postdoctoral Researchers who are currently either faculty members of world-leading universities, affiliated with prestigious corporations, or successful entrepreneurs.

Dr. Dai is a Fellow of the Royal Academy of Engineering (FREng), and a Member of Academia Europaea (MAE). He is an Editor-in-Chief of ROBOTICA, a Subject Editor of Mechanism and Machine Theory, and the IFToMM U.K. Board Chair. A pioneering figure in reconfigurable mechanisms and robots, origami robots, ankle rehabilitation robots, metamorphic robots and an expert in Theoretical Kinematics, he was the 27th recipient of the ASME DED Mechanisms and Robotics Award since 1974, the 58th recipient of the ASME Machine Design Award since 1958, the 15th of the IFToMM Award of Merits since 2003 in addition to receiving other awards including the AT Yang Award in Theoretical Kinematics in 2019, the Crossley Award in 2018, the 2010 King's College London Overall Supervisory Excellence Award.